

# Microlensing Surveys for Exoplanets

B. Scott Gaudi

Department of Astronomy, The Ohio State University, Columbus, Ohio 43210;  
email: gaudi@astronomy.ohio-state.edu

Annu. Rev. Astron. Astrophys. 2012. 50:411–53

First published online as a Review in Advance on  
June 15, 2012

The *Annual Review of Astronomy and Astrophysics* is  
online at [astro.annualreviews.org](http://astro.annualreviews.org)

This article's doi:  
10.1146/annurev-astro-081811-125518

Copyright © 2012 by Annual Reviews.  
All rights reserved

0066-4146/12/0922-0411\$20.00

## Keywords

Galactic Bulge, gravitational microlensing, low-mass stars, planetary  
systems, variables

## Abstract

Unlike most other planet-detection techniques, gravitational microlensing does not rely on detection of photons from either the host or the planet. Rather, planets are discovered by their gravitational perturbation of light from a more distant source. I review the fundamental concepts of microlensing planet searches and discuss their practical application. I show how the strengths and peculiarities of the method flow from the basic manner in which planets are discovered. In particular, microlensing is sensitive to very low-mass planets on wide orbits and free-floating planets, and can be used to search for planets orbiting host stars with a broad range of masses and Galactocentric distances. However, microlensing events are rare and cannot be predicted in advance, the majority of the host stars are extremely faint, and the planetary signals typically last less than a day. These strengths motivate microlensing searches as powerful, complementary probes of unexplored parameter space that have already provided important constraints on the demographics of planets beyond the “snow line.” However, the real-world challenges associated with the practical application of the method have driven the organization and evolution of the microlensing field and will continue to drive future developments from next-generation ground-based experiments through possible future space-based missions.

#### Snow line:

the location in the protoplanetary disk where the disk midplane temperature is below the sublimation temperature of water

#### Angular Einstein

ring radius: the radius of the ringlike image of a source star created when a lens is located exactly along our line of sight to the source

## 1. INTRODUCTION

When a foreground lens star or remnant happens to pass close to our line of sight to a more distant source star, its gravitational field will perturb the light rays from the source, creating multiple images and resulting in a time-variable magnification of the source: a microlensing event. Planetary companions to the foreground lens that happen to be located near the paths of these images will create an additional perturbation to the source flux, enabling the detection of the planet. Planets can be detected also as isolated lenses arising from free-floating or very wide-separation planets. This unique way in which the microlensing method detects planets results in both advantages and disadvantages relative to other methods. Although the advantages provide strong motivation to develop the method, the peculiarities with its application and the intrinsic disadvantages have driven the organization and evolution of the field and will likely continue to largely dictate its future path.

The most important attributes of the microlensing method are (*a*) its sensitivity to planets orbiting host stars with a broad range of masses located over a large range of Galactocentric distances; (*b*) its sensitivity to low-mass planets, planets in wide orbits, free-floating planets, and in particular planets with orbits at or beyond the so-called snow line (the location in the protoplanetary disk where the disk midplane temperature is below the sublimation temperature of water); and (*c*) the fact that microlensing events and planetary perturbations are stochastic, rare, and unpredictable.

Because it relies on the direct gravitational influence of a planet, the microlensing method does not require the detection of flux from the planet or its host star. This contrasts to most other proposed or realized planet detection methods. As a result, microlensing is sensitive to a very broad range of host masses, including brown dwarfs, main-sequence stars, and stellar remnants. Furthermore, these hosts are typically located anywhere from a few hundred parsecs from the Sun to the Galactic center. Thus, microlensing is uniquely capable of constraining the demographics of planetary systems throughout the Galaxy, as opposed to most other techniques, which are typically strongly biased toward brighter and, therefore, more luminous or nearby host stars. However, the flipside is that the host stars of planets detected by microlensing are distant and faint, thus requiring substantial additional effort to characterize their properties. This has motivated the development of the use of higher order effects in microlensing events to help characterize the properties of the hosts, as well as space-based imaging to uniquely isolate host star light from the background stars in the crowded fields targeted by microlensing searches. Ultimately, the need to characterize microlensing host stars is one of the primary motivations of a space-based microlensing mission.

Microlensing detects planets through the instantaneous gravitational perturbation of the light rays of a source star by the planet, as opposed to methods such as radial velocity or astrometry, which require a full planet orbit to detect the gravitational influence of the planet on its host star. Furthermore, when detected in conjunction with the microlensing event caused by its host star, planets typically perturb light rays that pass close to the angular Einstein ring radius of the host lens,

$$\theta_E \equiv \left( \frac{4GM}{D_{\text{rel}}c^2} \right)^{1/2}, \quad (1)$$

where  $M$  is the mass of the (host) lens,  $D_{\text{rel}}^{-1} \equiv D_l^{-1} - D_s^{-1}$ , and  $D_l$  and  $D_s$  are the distances to the lens and source. For typical source and lens distances, this corresponds to a physical distance at the location of the lens of  $r_E \equiv \theta_E D_l \simeq [2 - 4] \text{ AU} (M/M_\odot)^{1/2}$ . This compares to the location of the snow line of  $\sim 2.7 \text{ AU} (M/M_\odot)$ . Thus, microlensing is sensitive to planets just beyond the snow line, a region that has considerable import for some planet formation theories. Furthermore, this region is more difficult to probe with other methods, particularly for low-mass host stars.

However, because the planetary perturbations do not repeat, depend only on instantaneous projected separation of the planet in units of  $\theta_E$ , and typically last only a very small fraction of the planet's orbital period, microlensing generically provides very little information about planet orbits. This fact has driven the search for the small but occasionally detectable effects of the orbital motion of the planet during the relatively brief planetary perturbations.

Microlensing relies on the chance alignment between a planet and a background star, a rare and stochastic event that cannot be predicted in advance. The microlensing event rate scales roughly as the product of the surface density of lenses and sources. It is thus generally maximized in regions of very high stellar surface density, and as a result the majority of microlensing surveys take place toward the Galactic center. The crowded nature of the fields increases photometric noise and also leads to the requirement of very high angular resolution imaging for unambiguous detection of light from the lens. The alignment required for a microlensing event is sufficiently precise that, even toward the Bulge, a random source star is only lensed by a foreground star once per several hundred thousand years. Thus, hundreds of millions of source stars must be monitored to detect the  $\sim 1,000$  microlensing events per year that are currently being found. Given their smaller angular Einstein ring radius, planetary perturbations are tens to hundreds of times rarer still. Detecting planets orbiting stars giving rise to microlensing events therefore requires surveying large areas of the sky in very crowded fields to detect the stellar events, and it requires continuous, high-cadence monitoring of those events to detect the planetary perturbations. As we discuss in Section 3, the precise realization of the monitoring programs needed to detect planets with microlensing depends on the kinds of planets one hopes to detect, has evolved considerably over the past twenty years, and will continue to evolve with the development of technology and the push to explore new areas of parameter space.

Microlensing searches for planets began in earnest in 1995, with the first detection in 2003. To date, 14 planets have been announced, with many more currently being analyzed and prepared for publication. Although only a few planets have been found, microlensing surveys have already provided important constraints on the frequency of cold terrestrial planets, giant planets, and Solar System analogs. Microlensing planet searches are currently transitioning to a next-generation model, representing a fundamentally different mode of operation, which should yield a nearly order-of-magnitude increase in the rate of detections relative to the first surveys. Space-based surveys will provide still larger detection rates, have sensitivity to a much larger region of parameter space, and will yield host star masses and distances for a large fraction of the detected events. Ultimately, the returns from next-generation surveys, when combined with the results from other complementary surveys such as *Kepler*, can paint a nearly complete picture of the demographics of planetary systems throughout the Galaxy.

The goal of this review is to summarize the theoretical foundation and salient properties of the microlensing method of searching for planets, show how the basic advantages and disadvantages of microlensing surveys flow from these properties, and then describe how these strengths and weaknesses have driven the organization and historical evolution of the microlensing field and will continue to drive future developments from next-generation ground-based experiments through possible future space-based missions. It is worth emphasizing some things this review is not meant to accomplish. In particular, given the limited space, this review is not meant to be a comprehensive or encyclopedic summary of the field. Furthermore, this review does not attempt to delve deeply into the (extremely rich) theory and phenomenology of planetary microlensing. Therefore, this review should not be seen as an instruction manual or primer on planetary microlensing. Rather, our goal is to provide a broad-brush picture of the salient properties and motivating influences of a dynamic and rapidly evolving field that is just beginning to reach maturity and is currently in transition to the next generation.

---

**Lens equation:** the equation relating the angular separation between the lens and source in the absence of lensing to the angular positions of the images of the source created for a foreground mass acting as a gravitational lens

---

Fortunately, there exist several reviews that, together, do provide a much more complete account of the field, and we refer the reader to these for more detailed information. In particular, comprehensive reviews are provided by Gaudi (2010) and Bennett (2008), where the former focuses on the theory and phenomenology of planetary microlensing, and the latter provides a more detailed motivation for space-based microlensing missions. Naturally, the current review borrows considerably from Gaudi (2010). In addition, *Gravitational Lenses* by Schneider, Ehlers & Falco (1992) is a standard reference for all things related to gravitational lensing. The monograph by Petters, Levine & Wambsganss (2001) delves into the rich mathematical underpinnings of gravitational lensing. The reader may also wish to refer to excellent reviews of gravitational microlensing by Paczyński (1996), Sackett (1999), and Mao (2008) for additional information.

We begin in Section 2 by providing a review of the fundamentals, strengths, and weaknesses of the microlensing method. In Section 3, we use this background to frame a discussion of the logistical implementation of microlensing surveys, discussing how these surveys have evolved and will continue to evolve over the next decade. In Section 4, we discuss various methods to characterize planetary systems detected with microlensing. In Section 5, we provide a brief historical overview of microlensing surveys for planets, and in Section 6, we summarize the results that have been obtained to date from these surveys, emphasizing what has been learned about the demographics of planets beyond the snow line. Finally, in Section 7, we conclude with a summary of possible future directions for the field, speculating on the expected returns from next-generation surveys over the next decade.

## 2. BASICS OF THE MICROLENSING METHOD

This section reviews the basic principles of the microlensing planet detection method. We first summarize the fundamental equations, characteristic scales, and observable features of both single and binary microlensing events; we go on to discuss the microlensing event rate; and finally, we summarize the strengths and weaknesses of the method.

### 2.1. The Lens Equation for a System of Point Mass Lenses

A microlensing event occurs when a lens happens to pass very close to our line of sight to a more distant source. The gravity of the lens deflects the light rays from the source, resulting in multiple images and a transient net increase of the source flux. As discussed in Section 2.5, the microlensing event rate for any given source is extremely small, but is maximized toward regions with a high surface density of lenses. As a result, most microlensing planet surveys target the very dense stellar regions toward the Galactic center. Therefore, the sources we consider are typically main-sequence or giant stars in the Bulge. The lenses are representative of the population of compact objects along the line of sight toward the Bulge, and so are typically stars or remnants in the Galactic disk or foreground Galactic Bulge (see Sections 2.5 and 2.6.1).

The basic geometry of gravitational microlensing is shown in **Figure 1**. Consider a source star located at a distance of  $D_s$  and a closely aligned lens located at a distance  $D_l$ . Light rays from the source star passing by the lens will be bent by the gravity of the lens by an angle  $\hat{\alpha}_d$ . The lens equation relates the angular separation  $\beta$  between the lens and the source in the absence of lensing to the angular positions  $\theta$  of the images of the source that are displaced by an angle  $\alpha_d(\theta)$ ,

$$\beta = \theta - \alpha_d(\theta). \quad (2)$$

Using the small-angle approximation, the two deflection angles can be related,  $\hat{\alpha}_d(D_s - D_l) = \alpha_d D_s$ .

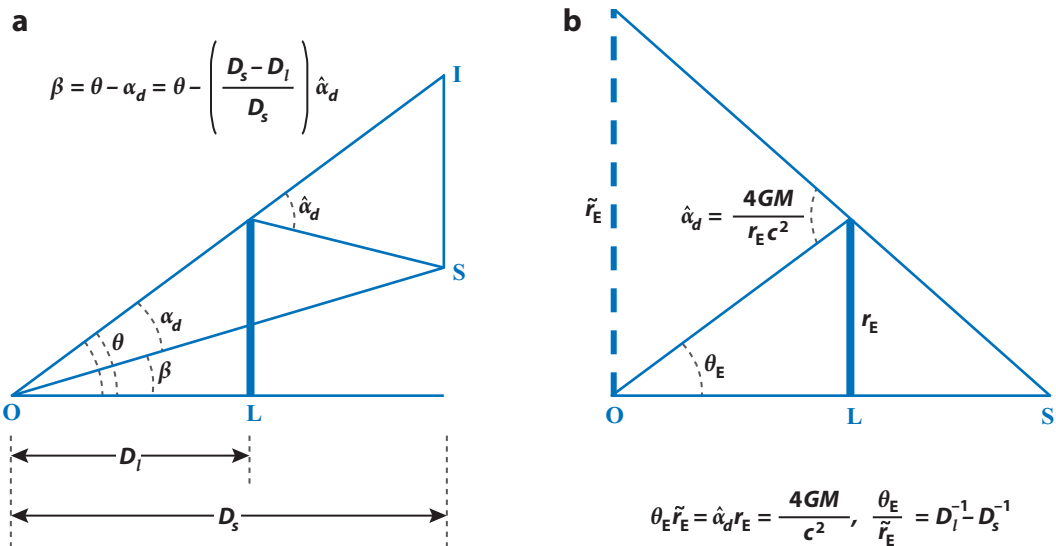


**Figure 1**

(a) The lens (L) at a distance  $D_l$  from the observer (O) deflects light from the source (S) at distance  $D_s$  by the Einstein bending angle  $\hat{\alpha}_d$ . The angular positions of the images  $\theta$  and unlensed source  $\beta$  are related by the lens equation,  $\beta = \theta - \alpha_d = \theta - [(D_s - D_l)/D_s] * \hat{\alpha}_d$ . For a point lens,  $\hat{\alpha}_d = 4GM/(c^2 D_l \theta)$ . (b) Relationship of higher order observables, the angular ( $\theta_E$ ) and projected ( $\tilde{r}_E$ ) Einstein radii, to physical characteristics of the lensing system. Adapted from Gould (2000b), reproduced by permission of the AAS.

According to general relativity, light rays passing a distance  $b$  from a lens of mass  $M$  will be bent by an angle (e.g., Schneider, Ehlers & Falco 1992),

$$\hat{\alpha}_d = \frac{4GM}{|b|^2 c^2} b. \quad (3)$$

For multiple lens masses, the deflections add vectorially. Thus, considering a lens consisting of  $N_L$  point masses all located on a plane at a distance  $D_l$ , each with mass  $m_i$  and angular position  $\theta_{m,i}$ , we can derive the total deflection angle of the system,

$$\alpha_d(\theta) = \frac{4G}{D_{\text{rel}} c^2} \sum_i^{N_L} m_i \frac{\theta - \theta_{m,i}}{|\theta - \theta_{m,i}|^2}, \quad (4)$$

where, as before  $D_{\text{rel}}^{-1} \equiv D_l^{-1} - D_s^{-1}$ , and we have used the fact that  $D_l \mathbf{b}_i = \theta - \theta_{m,i}$ . Given the masses and angular positions of the lenses and source, along with the distances to the source and lens plane, one can then use Equations 2 and 4 to solve for the image positions.

Gravitational lensing can also be thought of as the mapping  $\beta \rightarrow \theta$  between the source plane and lens plane under the action of the gravitational lens. This mapping is generally not one-to-one, with multiple image positions typically created for each source position. This mapping also results in distorted images whose areas may differ from that of the unlensed source. Because lensing conserves surface brightness, and the observed flux from an image is just the surface brightness integrated over the image area, the flux of the images will not necessarily be equal to the unlensed flux of the source. In other words, the images are either magnified or demagnified. Because image distortions are caused by the lens mapping given by the lens equation (Equation 2) for a small source, the magnification  $A_j$  of each image  $j$  is given by the inverse of the determinant of the

**Caustic curves:** the set of all positions of the source where the determinant of the Jacobian of the mapping from image to source positions given by the lens equation vanishes

**Critical curves:** the images of the caustic curves

Jacobian of the lens equation evaluated at the image position  $j$ ,

$$A_j = \frac{1}{\det J} \Big|_{\theta=\theta_j}, \quad \det J \equiv \left| \frac{\partial(\beta_1, \beta_2)}{\partial(\theta_1, \theta_2)} \right|. \quad (5)$$

One of the most important properties of gravitational lensing is that the mapping between the source and lens planes can be singular for some set of source positions, such that  $\det J = 0$  at these positions. In other words, at these positions, an (infinitesimally small) area element in the source plane is mapped to an infinitely large area in the image position. For point sources at these positions, the magnification is formally infinite, and for finite-sized sources near these positions, the magnification is generally large. The set of all source positions where  $\det J = 0$  defines closed caustic curves, and the set of all image positions to which the caustics map defines closed critical curves.

## 2.2. Microlensing Events due to a Single Lens

In the case of a single lens mass, we can choose the position of the lens as the origin. Furthermore, we can recognize that, by symmetry, the lens, source, and images will all be colligned, and so drop the vector notation, keeping the convention that positive values of  $\theta$  correspond to images on the same side of the lens as the source. With these assumptions, the lens equation reduces to

$$\beta = \theta - \frac{4GM}{c^2 D_{\text{rel}} \theta}. \quad (6)$$

If the lens and source are exactly aligned,  $\beta = 0$ , the source is imaged into a ring of angular radius,

$$\theta_E \equiv \left( \frac{4GM}{D_{\text{rel}} c^2} \right)^{1/2}, \quad (7)$$

commonly called the angular Einstein ring radius. This angle defines the basic scale of gravitational microlensing. It is instructive to note several alternative forms for this quantity. In particular, we can write  $\theta_E = (2R_{\text{Sch}}/D_{\text{rel}})^{1/2}$ , where  $R_{\text{Sch}}$  is the Schwarzschild radius of the lens. We can also write,

$$\theta_E \equiv (\kappa M \pi_{\text{rel}})^{1/2}, \quad (8)$$

where  $\pi_{\text{rel}} = \text{AU}/D_{\text{rel}}$  is the relative lens-source parallax, and  $\kappa = 4G/(c^2 \text{AU}) = 8.144 \text{ mas } M_{\odot}^{-1}$ . Evaluating,

$$\theta_E = 713 \mu\text{as} \left( \frac{M}{0.5 M_{\odot}} \right)^{1/2} \left( \frac{\pi_{\text{rel}}}{125 \mu\text{as}} \right)^{1/2}. \quad (9)$$

At the distance of the lens, this corresponds to a linear Einstein ring radius of

$$r_E \equiv \theta_E D_l \quad (10)$$

$$= 2.85 \text{AU} \left( \frac{M}{0.5 M_{\odot}} \right)^{1/2} \left( \frac{D_s}{8 \text{kpc}} \right)^{1/2} \left[ \frac{x(1-x)}{0.25} \right]^{1/2}, \quad (11)$$

where  $x \equiv D_l/D_s$ .

Normalizing all angles by  $\theta_E$  and defining  $u = \beta/\theta_E$  and  $y = \theta/\theta_E$ , we can rewrite the single lens equation (Equation 6) in the exceptionally simple form,

$$u = y - y^{-1}. \quad (12)$$

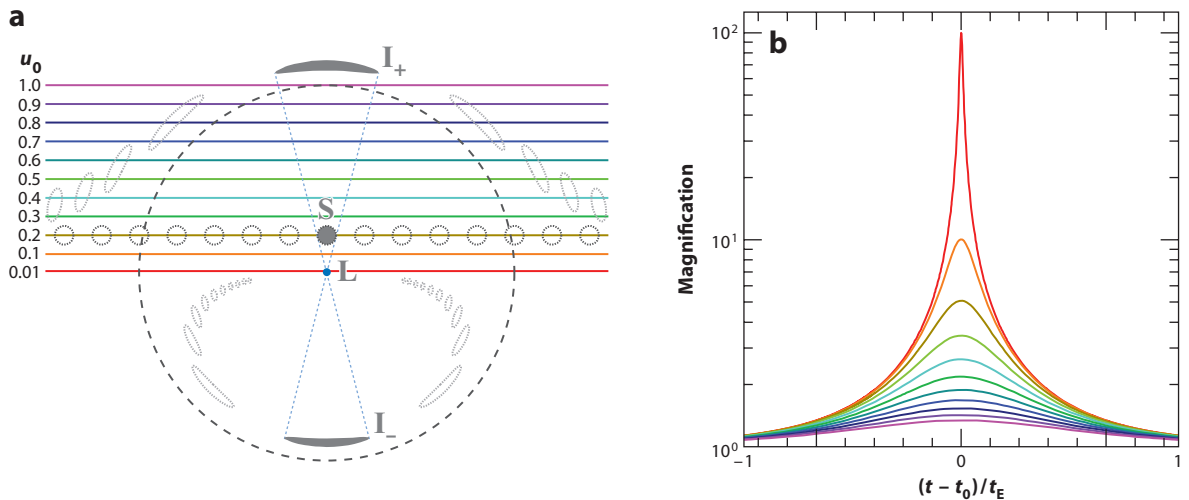


**Figure 2**

(a) All angles are normalized by the angular Einstein ring radius  $\theta_E$ , shown as a dashed circle of radius  $\theta_E$ . The shaded circle shows the source (S) at an angular separation of  $u = 0.2$  from the lens (L). The gray shaded arcs show the two images that are created, one outside the Einstein ring ( $I_+$ ) on the same side of the lens as the source with position from the lens of  $y_+ = 0.5(\sqrt{u^2 + 4} + u)$ , and one inside the Einstein ring on the opposite side of the lens as the source with position from the lens of  $y_- = -0.5(\sqrt{u^2 + 4} - u)$ . The images are compressed radially but elongated tangentially. Because surface brightness is conserved, the magnification of each image is just the ratio of its area to the area of the source. Because the images are typically unresolved, only the total magnification of the two images is measured, which depends only on  $u$ . The other circles and arcs show the source and images at different times for a trajectory with impact parameter  $u_0 = 0.2$ . (b) Magnification as a function of time (colored curves) for the ten trajectories shown in panel a with impact parameters  $u_0 = 0.01, 0.1, 0.2, \dots, 1.0$ . Time is relative to the time  $t_0$  of the peak of the event (when  $u = u_0$ ) and in units of the angular Einstein crossing time  $t_E$ . Higher magnification implies more elongated images, which leads to increased sensitivity to planetary companions. Adapted from Paczyński (1996).

This is equivalent to a quadratic equation in  $y$  with solutions,

$$y_{\pm} = \pm \frac{1}{2}(\sqrt{u^2 + 4} \pm u). \quad (13)$$

Thus, in the general case of imperfect alignment ( $u \neq 0$ ), a single lens produces two images. The positive solution (also called the major or minimum image) is located on the same side of the lens as the source and is always located outside the Einstein ring with  $y_+ > 1$ . The negative solution (also called the minor or saddle image) is located on the opposite side of the lens as the source and is always located inside the Einstein ring with  $|y_-| < 1$ . The angular separation between the two images on the sky is  $\Delta\theta = |y_+ - y_-|\theta_E = (u^2 + 4)^{1/2}\theta_E$ , and so is  $\lesssim 2\theta_E$  when  $u \lesssim 1$ . Given the typical lens masses of  $[0.1 - 1] M_{\odot}$  and distances of  $D_l = [1 - 7]$  kpc, and sources in the Galactic Bulge, the images are separated by the order of a milliarcsecond or less and, thus, are not resolved.

For a point lens, the magnification of each of the two images can be derived by evaluating the determinant of the Jacobian of the point lens equation evaluated at each image (Equation 5). However, the magnifications can also be determined by examining the geometry of the images in **Figure 2** and noting that, for a small source, the images will be elongated in the tangential direction relative to the source by an amount  $y_{\pm}/u$  but compressed radially by an amount  $dy_{\pm}/du$ , and thus the magnification of each image is,

$$A_{\pm} = \left| \frac{y_{\pm}}{u} \frac{dy_{\pm}}{du} \right| = \frac{1}{2} \left[ \frac{u^2 + 2}{u\sqrt{u^2 + 4}} \pm 1 \right]. \quad (14)$$



The total magnification is

$$A(u) = \frac{u^2 + 2}{u\sqrt{u^2 + 4}}. \quad (15)$$

Note that the magnification diverges for  $u = 0$ ; this point corresponds to the caustic for a single lens. The Einstein ring ( $y = 1$ ) corresponds to the critical curve. Several approximations of this equation are useful to note. For  $u \ll 1$ ,  $A \simeq 1/u$ , and for  $u \gg 1$ ,  $A \simeq 1 + 2u^{-4}$ . Note that as  $u \rightarrow \infty$ ,  $y_+ \rightarrow u$  and  $A_+ \rightarrow 1$ , and  $y_- \rightarrow 0$  and  $A_- \rightarrow 0$ ; i.e., as the source moves very far from the lens, the major image position and flux becomes coincident with that of the unlensed source, and the minor image position approaches that of the lens and its magnification goes to zero.

Because the observer, source, and lens are all in relative motion, the angular separation between the source and lens, and thus the magnification, will be a function of time, giving rise to a microlensing event. In the simplest case, the relative proper motion between the lens and source,  $\mu_{\text{rel}}$ , at the time of the event can be approximated to be constant; i.e., when the projected accelerations of the lens, source, and observer are small, the trajectory of the source relative to the lens can be assumed to be rectilinear,

$$u(t) = (\tau^2 + u_0^2)^{1/2}. \quad (16)$$

Here,  $\tau \equiv (t - t_0)/t_E$ ,  $u_0$  is the impact parameter of the event,  $t_0$  is the time of closest alignment when  $u = u_0$  (which is also the time of maximum magnification), and  $t_E$  is the Einstein ring crossing time,

$$t_E \equiv \frac{\theta_E}{\mu_{\text{rel}}}. \quad (17)$$

The magnification as a function of time for a single lens microlensing is thus described by a three-parameter ( $t_E$ ,  $t_0$ ,  $u_0$ ) family of curves. **Figure 2** illustrates the variety of light curve shapes by showing a series of such curves with a range of impact parameters, corresponding to maximum magnifications between  $A(1) = 3/\sqrt{5} \simeq 1.34$  and  $A(0.01) \simeq 1/0.01 = 100$ . The characteristic smooth, symmetric form for a single lens event is often called a “Paczynski curve” (Paczynski 1986).

Microlensing events toward the Galactic Bulge have a typical timescale of order a month,

$$t_E \simeq 24.8 \text{ days} \left( \frac{M}{0.5 M_\odot} \right)^{1/2} \left( \frac{\pi_{\text{rel}}}{125 \mu\text{as}} \right)^{1/2} \left( \frac{\mu_{\text{rel}}}{10.5 \text{ mas year}^{-1}} \right)^{-1}, \quad (18)$$

but owing to the large range of lens masses and distances, and source and lens velocities, the observed timescale distribution is quite broad, ranging from a few days to a few years (see Section 2.5 and **Figure 3**)

### 2.3. $N$ -Point Mass Lenses

A lens star with a planet constitutes a special case of a binary lens ( $N_l = 2$ ) with an extreme mass ratio between the two components. Of course, stars can host multiple planets, planets exist in binary star systems, and planets have moons. Therefore, we should also be able to determine the properties of higher order systems of lenses with  $N_l > 2$ .

To derive the microlensing properties of such systems, we begin with the lens equation for a system of  $N_l$  point mass lenses derived previously (Equations 2 and 4). We can simplify these equations by first normalizing all angles to a common scale. The choice of this scale is arbitrary, but for many geometries the most sensible choice is the angular Einstein ring radius of the total lens mass  $M_{\text{tot}} \equiv \sum_i^{N_l} m_i$ . As with the single lens, we can then define a dimensionless vector source position  $\mathbf{u} \equiv \boldsymbol{\beta}/\theta_E$ , and dimensionless vector image positions  $\mathbf{y} \equiv \boldsymbol{\theta}/\theta_E$ . We can then write



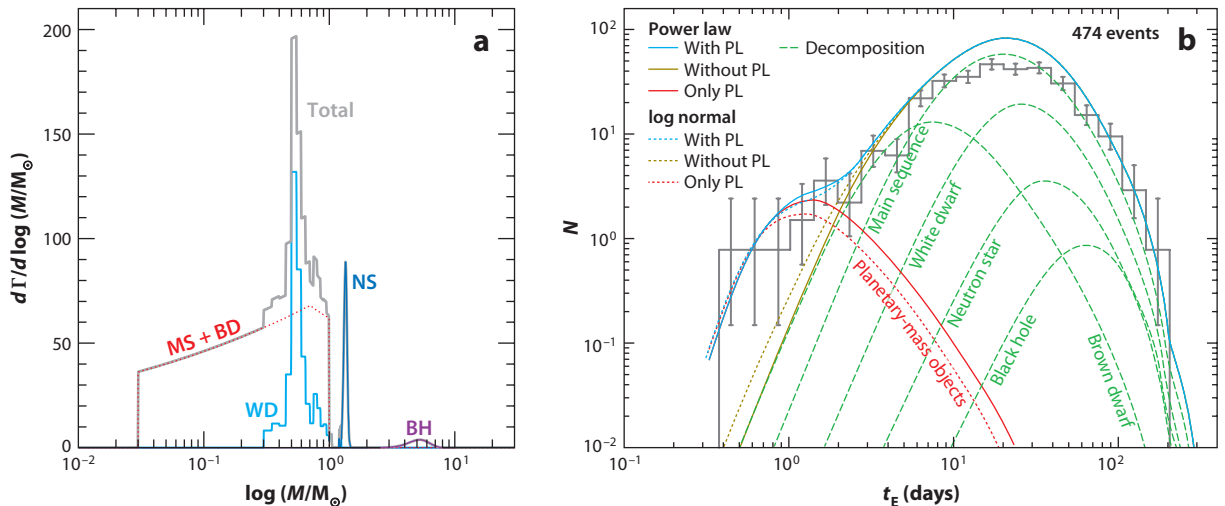


**Figure 3**

(a) Example theoretical estimate of the rate of microlensing events toward the Galactic Bulge as a function of the mass of the lens, for main-sequence (MS) stars, brown dwarfs (BD,  $0.03 M_\odot < M < 1 M_\odot$ ) and white dwarfs (WD), neutron stars (NS), and black hole (BH) remnants. The total is shown by the thick gray solid curve. Adapted from Gould (2000a), reproduced by permission of the AAS. (b) Observed distribution of microlensing event timescales from the MOA collaboration during 2006–2007. The dark yellow solid and dotted curves show two model fits to this timescale distribution. The decomposition of one of these into the contribution of lenses of different ranges of masses using a model similar to that adopted by Gould (2000a) in panel *a* is indicated by the dashed green lines. There is a clear excess of events with  $t_E \sim 2$  days over this model fit, suggesting a population of wide-separation or free-floating planetary-mass objects (Sumi et al. 2011). The solid and dotted blue curves show a model fit to the timescale distribution including this population, which is shown in the solid and dotted red curves. Adapted from Sumi et al. (2011).

the lens equation as

$$\mathbf{u} = \mathbf{y} - \sum_i^{N_l} \epsilon_i \frac{\mathbf{y} - \mathbf{y}_{m,i}}{|\mathbf{y} - \mathbf{y}_{m,i}|^2}, \quad (19)$$

where  $\epsilon_i \equiv m_i/M_{\text{tot}}$ , and  $\mathbf{y}_{m,i}$  is the position of lens mass  $i$ .

It proves to be quite useful to write the lens equation in complex coordinates (Witt 1990). Defining the components of the (dimensionless) source position to be  $\mathbf{u} = (u_1, u_2)$  and the image position(s) to be  $\mathbf{y} = (y_1, y_2)$ , the two-dimensional source and images positions can be expressed in complex form as  $\zeta = u_1 + iu_2$  and  $z = y_1 + iy_2$ . The lens equation can now be rewritten:

$$\zeta = z - \sum_i^{N_l} \frac{\epsilon_i}{\bar{z} - \bar{z}_{m,i}}, \quad (20)$$

where  $z_{m,i}$  is the complex position of mass  $i$ . By taking the complex conjugate of Equation 20, one can obtain an expression for  $\bar{z}$ . Substituting this back into Equation 20 and clearing fractions yields a complex polynomial of order  $N_l^2 + 1$  with  $N_l^2 + 1$  roots. These roots can then be found with standard numerical routines, e.g., the ZROOTS subroutine from Press et al. (1992), which uses Laguerre's method. However, it is important to note that the solutions to this complex polynomial are not necessarily solutions to the lens equation, and thus the trial roots of the polynomial must be substituted back into the lens equation to find the true image positions  $z_j$ . Depending on the location of the source with respect to the lens positions, several of the images may be spurious. In fact, it has been shown that the maximum number of images is  $5(N_l - 1)$  for  $N_l \geq 2$  [S. H. Rhie,

### Fold and cusp

**caustics:** caustics are generically composed primarily of curved, concave fold sections that meet at points called cusps

unpublished work (astro-ph/0103463, astro-ph/0305166); Khavinson & Neumann 2006]. Thus, for  $N_l > 3$ , it is always the case that some of the roots of the polynomial are not solutions to the lens equation.

In complex coordinates, the determinant of the Jacobian is

$$\det J = 1 - \frac{\partial \zeta}{\partial \bar{z}} \frac{\partial \bar{\zeta}}{\partial z}, \frac{\partial \zeta}{\partial \bar{z}} = \sum_i^{N_l} \frac{\epsilon_i}{(\bar{z} - \bar{z}_{m,i})^2}, \quad (21)$$

and the magnification of the individual images can be found by evaluating the (inverse) of the Jacobian determinant at the image positions (Equation 5). Note that the resulting image magnifications can be positive or negative, where the sign corresponds to the parity (handedness) of the image. Because the images are typically unresolved, we measure the total magnification:  $A \equiv \sum_j |A_j|$ .

The critical curves correspond to the set of image positions where  $\det J = 0$ . By inspecting Equation 21, this condition is given by

$$\left| \sum_i^{N_l} \frac{\epsilon_i}{(\bar{z} - \bar{z}_{m,i})^2} \right|^2 = 1. \quad (22)$$

A simple way of finding the critical curves can be found by noting that the sum in Equation 22 must have a modulus equal to unity. Therefore, we can solve for the critical image positions parametrically by solving the equation,

$$\sum_i^{N_l} \frac{\epsilon_i}{(\bar{z} - \bar{z}_{m,i})^2} = e^{i\phi}, \quad (23)$$

for each value of the parameter  $\phi = [0, 2\pi)$  (Witt 1990). The set of points on the critical curve can then be inserted into the lens equation (Equation 20) to determine the set of source positions where  $\det J = 0$  and, thus, where the magnification of a point source is formally infinite. The set of such source positions (corresponding to the mapping of the critical curve image positions) defines the closed caustic curves. By clearing the complex conjugates  $\bar{z}$  and fractions, Equation 23 can be written as a complex polynomial of degree  $2N_l$  (Witt 1990), and so there are at most  $2N_l$  critical curves and caustics.

For systems of point masses, caustic curves are characterized by multiple concave segments called folds that meet at points called cusps. Fold and cusp caustics have the useful property that the positions and magnifications of the critical images (the images that disappear when the source crosses the caustic) of sources near folds and cusps have universal scaling behaviors that can be described essentially analytically, and whose normalization depends only on the local properties of the lens potential. This universal and local behavior of the magnification near caustics has proven quite useful, in that it allows one to understand and analyze light curves near caustic crossings separate from, and independent of, the global lens model.

The magnification of a source of finite size begins to deviate by more than a few percent from the point-source approximation when the center of the source is within several source radii of a caustic singularity. Note this includes the caustics created in binary lenses, but also includes the point caustic located at the location of the lens for an isolated lens star or isolated planet. Although the magnification of a finite source can be found by integrating the surface-brightness-weighted point-source magnification over the source, this approach is not very practical. More practical approaches involve integrating in the image plane, where the surface brightnesses are smooth and continuous.

There exists an extensive literature on the lensing behavior of sources near folds and cusps, as well as on robust and efficient algorithms to compute the magnification for finite sources. We

refer the reader to a more complete discussion and list of appropriate references for both of these topics in section 2.2.4 of Gaudi (2010).

## 2.4. Planetary Microlensing

For a binary lens ( $N_l = 2$ ), the lens equation is

$$\zeta = z + \frac{\epsilon_1}{\bar{z}_{m,1} - \bar{z}} + \frac{\epsilon_2}{\bar{z}_{m,2} - \bar{z}}. \quad (24)$$

This can be written as a fifth-order complex polynomial in  $z$ . The coefficients of the polynomial are given in Witt & Mao (1995). Polynomials of order higher than four cannot be solved analytically, and thus the roots must be determined numerically. Depending on the location of the source with respect to the positions of the lenses, two of the solutions to the polynomial do not solve the lens equation, and thus are spurious. Therefore, there are either two or three images.

The boundaries of the regions in the source plane where there are either three or five images are the caustic curves, and a binary lens has one, two, or three closed, nonintersecting caustic curves. Because the curves are nonintersecting, the number of images changes by exactly two when the source crosses a caustic of a binary lens. Which of these three topologies is realized, as well as the precise shape and size of the caustics, depends on two parameters, which are typically taken to be the mass ratio,  $q \equiv m_1/m_2$ , and the instantaneous projected separation of lens masses in units of  $\theta_E$  for the total mass,  $s \equiv |z_{m,1} - z_{m,2}|$ . Expressions for the critical values of  $s$  for which the topology changes for arbitrary  $q$  are given in Erdl & Schneider (1993).

**2.4.1. Caustics of planetary microlenses.** The structure of the caustics plays a central role in the phenomenology of planetary microlensing light curves and, thus, the detectability of planets with the microlensing method. For lenses consisting of a star orbited by a planet, i.e., binary lenses with a small mass ratio  $q$ , the overall magnification pattern and, thus, light curve produced by the lens is dominated by the host star; the planet typically produces perturbations to the magnification pattern that are localized to relatively small regions inside and proximate to the caustics. A source must cross close to one of these regions of perturbations to create a detectable signal, and thus the size, shape, and location of the caustics largely dictates the signal magnitude, form, and detection probability for a given planet. The caustic properties also affect the practical implementation of searches for planets of various masses and separations. Thus, an understanding of the positions, shapes, and sizes of the caustics produced in planetary lenses, and how these vary with the mass ratio  $q$  and projected separation  $s$  of the planet, provides the key theoretical context for understanding the microlensing detection method and microlensing planet searches in general.

**Figure 4** shows the caustics of a binary lens corresponding to a planet/host mass ratio of  $q = 0.003$ , similar to that of Jupiter and the typical microlensing host of mass  $0.5 M_\odot$ . The caustics are shown for a range of values  $s$  spanning the three different caustic topologies. For small mass ratios  $q \ll 1$ , the boundaries between these topologies for a given  $q$  are  $s_c \simeq 1 - 3q^{1/3}/4$  and  $s_w \simeq 1 + 3q^{1/3}/2$  (Dominik 1999). These three regimes are typically referred to as the close ( $s < s_c$ ), intermediate or resonant ( $s_c < s < s_w$ ), and wide ( $s > s_w$ ) topologies. Thus, for small mass ratios, the intermediate topology is only realized for a relatively narrow range of projected separations spanning the Einstein ring of width  $s_w - s_c \simeq 9q^{1/3}/4$ , with this range shrinking for decreasing planet mass ratios as  $q^{1/3}$ .

As shown in **Figure 4**, for both the close and wide topologies of planetary lenses, there exists an arrowhead-shaped caustic with four cusps that is always located close to the position of the host star. This is known as the central caustic. The central caustic has two on-axis cusps and two

---

**Central caustics:** one of the two classes of caustics produced by planetary lenses whose projected separations are not close to  $\theta_E$ ; are always located near the primary and probed in high-magnification events

---

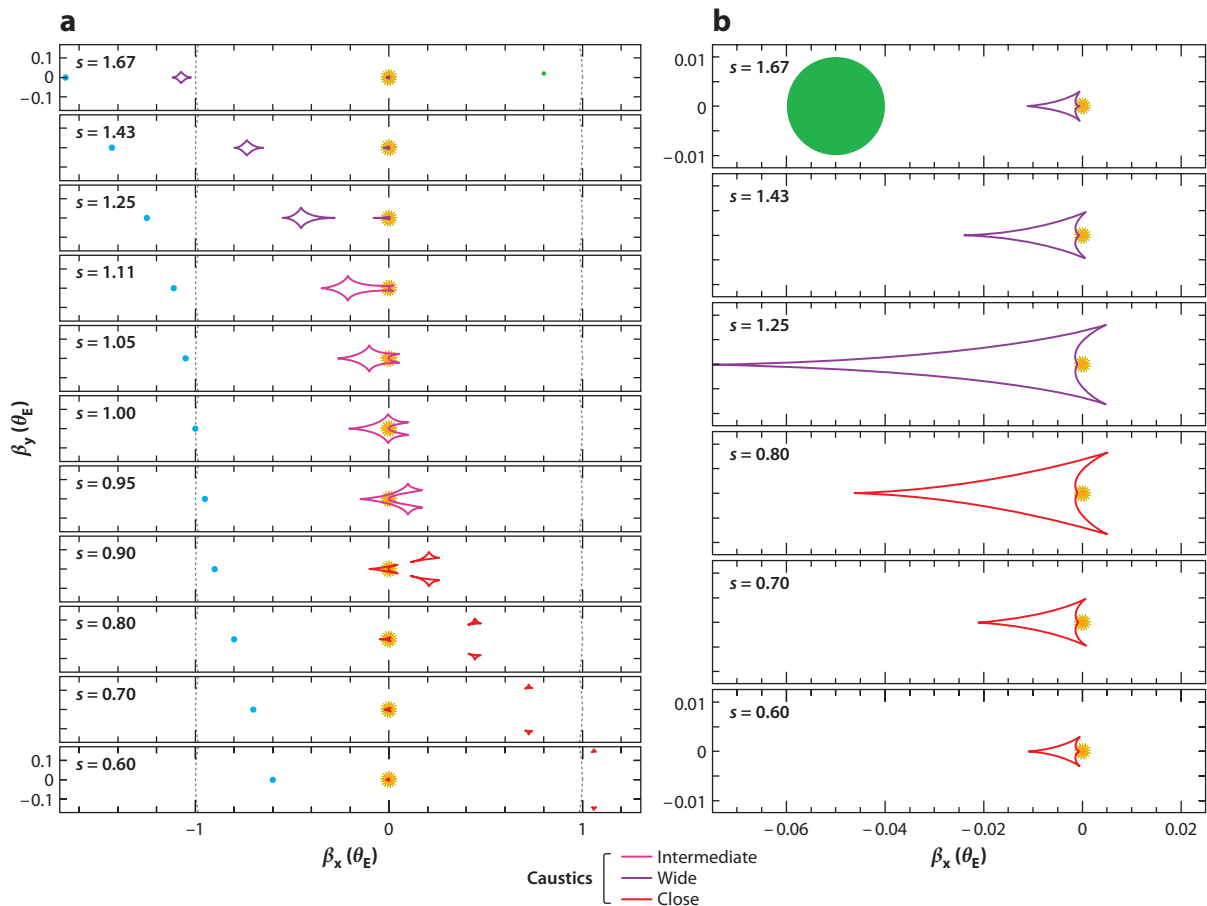


**Figure 4**

(a) The red, magenta, and purple curves show the caustics for a planetary lens with mass ratio  $q = 0.003$ , and various values of  $s$ , the projected separation in units of  $\theta_E$ . The dotted gray lines show sections of the Einstein ring. The light blue dots show the location of the planet. The host star is located at the origin of all the graphs as a Sun symbol. In the topmost graphs of both panels *a* and *b*, a representative angular source size in units of  $\theta_E$  of  $\rho = 0.01$  is shown as a green dot, corresponding to a star with radius of  $\sim 13 R_\odot$  (i.e., a clump giant) in the Galactic Bulge. (b) Zooms of the central caustics for several values of  $s$  for the planetary lenses shown in graphs in panel *a*. Trajectories that probe the central caustic correspond to events with small impact parameter  $u_0$  or events with high maximum magnification  $s \leftrightarrow s^{-1}$ , particularly for  $s \ll 1$  and  $s \gg 1$ . The degree of asymmetry, i.e., the length-to-width ratio, of the central caustic depends on  $s$ , such that the caustic becomes more asymmetric as  $s \rightarrow 1$ . Both figures adapted from *Exoplanets*, edited by Sara Seager. ©2012 The Arizona Board of Regents. Reprinted by permission of the University of Arizona Press.

off-axis cusps, with the cusp corresponding to the tip of the arrow pointing toward the planet. Sources passing roughly perpendicular to the planet/star axis near the tip of the central caustic result in a positive perturbation from magnification due to the host star. Sources passing roughly perpendicular to the axis but on the opposite side of the caustic, near the “back end” of the arrowhead, result in a negative, trough-shaped perturbation from the single lens curve.

In the limit of  $q \ll 1$  and  $|s - 1| \gg q$ , the size of the caustic scales as  $q$  for fixed  $s$ , and the degree of asymmetry of the caustic depends only on  $s$ , increasing as  $s \rightarrow 1$ . Also in this limit, the size and shape of the caustics are invariant under the transformation  $s \leftrightarrow s^{-1}$

(see **Figure 4**). This degeneracy arises from symmetries in the lens equation itself and applies to the lensing properties of the system in general for sources near the central caustic (Dominik 1999). This close/wide degeneracy generally becomes more perfect for  $q \ll 1$  and  $s \ll 1$ . Thus, it is difficult to distinguish between very close and/or very wide, low-mass planets detected through central caustic perturbations.

Because the central caustic is generally small and always located near the primary, planets are detected through perturbations from the central caustic only when the source passes relatively close to the primary, i.e., in high-magnification events with  $u_0 \ll 1$ . Because the intrinsic distribution of  $u_0$  is uniform, such events are relatively rare. However, searching for planets through this high-magnification event channel has several advantages. First, the perturbations due to central caustics are localized near the peak of the event, typically within the span of the full-width at half-maximum centered on the peak,  $\Delta t_{\text{FWHM}} \simeq \sqrt{12} u_0 t_E$ , corresponding to  $\lesssim 2$  days for typical high-magnification events. Second, with a fair amount of effort, high-magnification events can, in principle, be predicted in advance of their peak magnification. Third, the high magnification of the source generally results in improved photometry because of both the high photon flux and also confusion due to nearby stars (typically referred to as blending) is less important. In particular, high-magnification events can often be monitored with relatively small telescopes, with apertures of 0.5 m or less.

For the close topology  $s < s_c$ , there are three caustic curves (see **Figure 4**). In addition to the central caustic, there are two, larger triangular-shaped caustics located symmetrically on opposite sides of the planet-star axis. These caustics are referred to as the planetary caustics, as they are associated with the planet rather than the star. The size of these caustics scale as  $q^{1/2} s^3$ , and the separation between them (perpendicular to the planet-star axis) is  $\sim 2q^{1/2}(s^{-2} - 1)^{1/2}$  (Han 2006), and thus these caustics move apart as  $s$  decreases for fixed  $q$ . The caustics are located a distance of  $u_c \simeq s^{-1} - s$  from the host star along the planet-star axis and are on the opposite side of the primary from the planet. The magnification pattern near the planetary caustics is characterized by small regions of positive deviation from the single lens magnification due to the host star that are confined to source locations interior and immediate to the caustics, and a large region of negative deviation located between the caustics.

For the wide topology  $s > s_w$ , there are two caustic curves (see **Figure 4**). In addition to the central caustic, there is one, larger, asteroid-shaped caustic with four cusps centered on the planet-star axis, which is also referred to as the planetary caustic. The size of the planetary caustic scales as  $\simeq q^{1/2} s^{-2}$ . The width of the caustic along the planet-star axis is generally larger than the width perpendicular to the axis, with the caustic becoming more symmetric for larger  $s$  (Han 2006). The planetary caustic is centered at a distance of  $u_c \simeq s - s^{-1}$  from the host star along the planet-star axis and is on the same side of the primary from the planet. The magnification pattern near the planetary caustic is characterized by lobes of positive deviation from the single lens magnification near the four cusps, with small regions of slight negative deviation just outside the fold caustics between the cusps.

For the intermediate topology ( $s_c < s < s_w$ ), there is one, relatively large caustic with six cusps. As can be seen in **Figure 4**, this caustic is formed as  $s$  approaches  $s_c$  from below or  $s$  approaches  $s_w$  from above when the planetary caustics merge with the central caustic (Wambsganss 1997). The size of the resonant caustic scales as  $q^{1/3}$  for fixed  $s$ . For a given mass ratio  $q$ , the intermediate (or resonant) caustic is larger than either the planetary or central caustics for arbitrary  $s$ . The large size of the resonant caustic results in a relatively large cross section, as well as perturbations that can last a significant fraction of the primary event timescale. However, these caustics are also relatively weak, in the sense that for a large fraction of the area interior to or immediately outside the caustic, the perturbation from the single lens magnification is small. The exceptions to this

#### High-magnification events:

events for which the source and lens reach a small minimum projected separation ( $\lesssim 0.01 \theta_E$ ) and, thus, the peak magnification is high ( $A_{\text{max}} > 100$ )

#### Planetary caustics:

one of the two classes of caustics produced by planetary lenses whose projected separations are not close to  $\theta_E$ ; generally probed in low-magnification events

**Finite source effects:**  
the deviation of the  
magnification from the  
point-source  
assumption due to the  
finite size of the source  
star; allows one to  
infer  $\theta_E$

are near the back end of the caustic, where there exists a strong trough of negative perturbation, and near the on-axis cusp at the front of the caustic, where there is a lobe of positive deviation. An important characteristic of resonant caustics is that their precise shape depends sensitively on  $s$  (see **Figure 4**). This property, combined with the fact that the deviations due to resonant caustics can last a relatively long time, implies that such events are more sensitive to small changes in  $s$  over the course of the perturbation arising from orbital motion of the planet.

As discussed above, one expects deviations from the point-source magnification due to the finite size of the source in regions where the magnification is a rapidly changing function of the source position and, in particular, for sources that are within a few source radii from a caustic curve. The magnitude of such finite source effects depend on the angular size of the source  $\theta_*$  in units of the angular Einstein ring radius,  $\rho \equiv \theta_*/\theta_E$ . For reference, a star of radius  $R_*$  located in the Galactic center with a distance of  $D_s = 8$  kpc has an angular size of  $\theta_* = 0.581 \mu\text{as}(R_*/R_\odot)$ , and for an angular Einstein ring radius of  $\sim 713 \mu\text{as}$  (Equation 9), this corresponds to dimensionless source sizes of  $\rho \sim 0.01$ ,  $\sim 0.002$ , and  $\sim 0.0008$  for a clump giant ( $R \sim 13 R_\odot$ ), subgiant ( $R \sim 3 R_\odot$ ), and main-sequence ( $R \sim 1 R_\odot$ ) sources, respectively. Finite source effects are particularly important for planetary microlensing because the caustics created in planetary lenses can be smaller than the typical source star size, thus leading to a suppression of the magnitude of the planetary deviation. Very roughly, one expects finite effects to become dominant when  $\theta_*$  is of order the angular Einstein ring radius of the planet,  $\theta_* \sim \theta_{E,p}$ , or  $\rho \sim q^{1/2}$ . Thus, we expect finite sources to become important for planet mass ratios of  $\sim 10^{-4}$  (roughly corresponding to the mass ratio between Neptune and a star of  $\sim 0.5 M_\odot$ ) for giant sources and  $4 \times 10^{-6}$  (roughly corresponding to the mass ratio between the Earth and  $0.5 M_\odot$ ) for subgiant sources. Lenses in the Galactic Bulge typically have smaller Einstein ring radii and, thus, are more sensitive to finite source effects for fixed planet mass ratios. When  $q^{1/2} \ll \rho$ , finite source effects strongly suppress the magnitude of the deviations. Thus, detection of planets of mass substantially lower than that of Earth generally requires monitoring main-sequence stars in the Bulge (Bennett & Rhie 1996).

**2.4.2. Planetary microlensing perturbations.** As discussed above, because light curves are simply one-dimensional slices through the source plane, and significant perturbations from the single lens magnification are localized to regions near the caustics, an analysis of morphology of the caustics provides a way to understand the phenomenology of the light curve perturbations due to planetary companions, and thus the various types of primary events in which planets can be detected. In particular, planets can be detected in only a few qualitatively different ways. First, planets can be detected at relatively low magnification of the primary if the source happens to cross the planetary caustic from either close ( $s < s_c$ ) or wide ( $s > s_c$ ) planets. Such perturbations are unpredictable. Second, planets can be detected near the peak of high-magnification events through the perturbations from the central caustic of close or wide planets. High-magnification events are relatively rare, but can be predicted in advance of peak. Third, planets can be detected at modest to high-magnification through perturbations from the single, relatively large resonant caustic, although such perturbations may be relatively weak. Finally, wide-separation or free-floating planets can be detected as isolated, short timescale events.

An alternative and complementary way to understand the phenomenology of planetary microlensing events is to consider the magnification and paths of the two images created during the primary microlensing event, recognizing that a planetary perturbation occurs when the planet creates an additional, relatively short-lived distortion to one or both of these images. **Figure 5** shows the images, caustics, and light curves for three representative events that serve to illustrate the first three classes of planetary perturbations discussed above (planetary, central, and resonant caustic events). Free-floating planets obviously behave exactly as events due to isolated stars, except



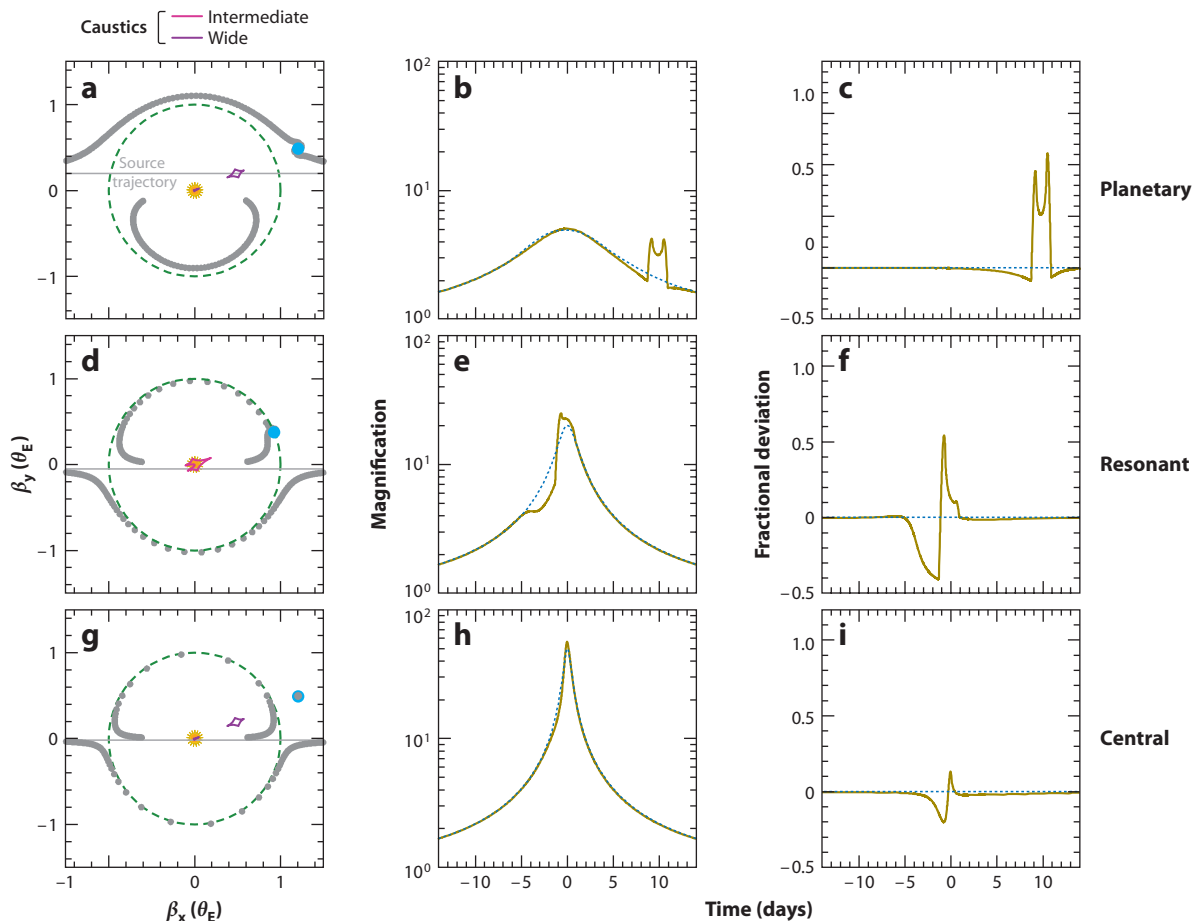


**Figure 5**

Image positions, caustics, and light curves for representative events that serve to illustrate the three classes of planetary perturbations to primary events: (a,b,c) planetary, (d,e,f) resonant, and (g,h,i) central. (a,d,g) The source trajectory is shown as a gray horizontal line, caustics in magenta and purple, and image positions in gray. The primary is located at the origin, as indicated by the Sun symbol; the planet with a mass ratio  $q = 0.003$  is located at  $s = 1.3$  in panels a and g and at  $s = 1.0$  in panel d, as indicated with the light blue circle. The Einstein ring radius of the primary is indicated with the green dashed circle. (b,e,h) Light curves for the unperturbed primary (dark blue dotted line) with the planetary perturbation (dark yellow line), assuming a typical timescale of  $t_E = 20$  days. (c,f,i) Fractional deviation of the light curve with the planetary perturbation from the magnification due solely to the primary. For all light curves, a finite source size of  $\rho = 0.01$  was assumed, corresponding to a clump giant in the Bulge for typical parameters.

for having shorter timescales on average. Events arising from very wide separations behave almost identically to those from isolated events, although there are potentially observable differences (Han et al. 2005).

Consider planets detected via the planetary caustic at relatively low magnification (Figure 5a,b,c). In isolation, the primary lens creates two images, which sweep out a path on the sky over the course of the primary event. The path of the major image is entirely contained outside the Einstein ring radius, and the path of the minor image is entirely contained within the Einstein ring radius. If the lens has a planetary companion, which happens to have a projected position near one of these two paths at the time of the event as the image sweeps by the position of



the planet, the planet further distorts the image (the other image is essentially unaffected), creating a brief perturbation. For a planet located exactly at the position of one of the images,  $s = y_{\pm}$ , and thus the caustic is centered a distance from the primary at the source position corresponding to the inversion of Equation 13, i.e.,  $u_c(y_{\pm} = s)$ , which yields  $u_c = |s - s^{-1}|$ . Planets inside the Einstein ring with  $s < s_c$  are perturbing the minor image ( $y_-$ ), and these typically provide an overall decrease in the size of this image, resulting in a net negative deviation from the primary lens magnification. Planets outside the Einstein ring with  $s > s_w$  are perturbing the major image ( $y_+$ ), typically resulting in a positive deviation from the primary lens magnification (as shown in **Figure 5**).

For planetary caustic perturbations, the properties of the planet can be essentially “read off” of the observed light curve (Gould & Loeb 1992). The primary event can be characterized by three gross observable parameters, the time of peak magnification  $t_0$ , the peak observed magnification  $A_{\max}$ , and a measure of the duration of the event, such as the full-width at half-maximum  $\Delta t_{FWHM}$ . Ignoring, for the purposes of exposition, the possibility of blending of the light of the source with unlensed light,  $A_{\max}$  and  $\Delta t_{FWHM}$  can be related to the Einstein timescale  $t_E$  and impact parameter  $u_0$  via Equations 15 and 16. For high-magnification events ( $u_0 \ll 1$ ),  $u_0 \sim A_{\max}^{-1}$  and  $t_E \sim 12^{-1/2} \Delta t_{FWHM} u_0^{-1}$ . The gross features of the planetary perturbation can be characterized by the time of the perturbation  $t_{0,p}$ , the duration of the perturbation,  $\Delta t_p$ , and the peak fractional deviation from the single lens magnification  $\delta_p$ . For sources that are small compared to the size of the planetary Einstein ring, the duration of this deviation is roughly given by the time it takes the image to sweep by the position of the planet, and so depends on the single lens magnification as well as on the detailed geometry, but is generally of order the planet Einstein ring crossing time,  $\Delta t_p \sim t_{E,p} = q^{1/2} t_E$ , and thus  $q \sim (\Delta t_p / t_E)^2$ . Because the planet must be located near the position of one of the two images,  $s \simeq y_{\pm}[u_p] = \pm \frac{1}{2} [\sqrt{u_p^2 + 4} \pm u_p]$ , where  $u_p = \{u_0^2 + [(t_{0,p} - t_0)/t_E]^2\}^{1/2}$  is the position of the source at the planetary perturbation. The other parameter that can be inferred is the angle of planet/star projected axis relative to the source trajectory,  $\alpha \simeq \sin^{-1}(u_0/u_p)$ . The peak fractional deviation  $\delta_p$  specifies the precise location of the planet relative to the unperturbed image at the time of the perturbation. Thus,  $t_{0,p}$ ,  $t_{E,p}$ , and  $\delta_p$ , along with the properties of the unperturbed primary event, completely specify the underlying parameters  $q$ ,  $s$ , and  $\alpha$ , up to a twofold discrete degeneracy in  $s$ , corresponding to whether the planet is perturbing the major or minor image. However, as discussed above, these two situations result in very different types of perturbations and so are easily distinguished (Gaudi & Gould 1997b).

In reality, there can be complications to the above procedure, which can hamper the ability to accurately measure the planetary parameters, particularly for perturbations detected at relatively low signal-to-noise ratios. For example, if finite source effects are important but not dominant, then there exists a continuous degeneracy between the mass ratio and the finite source size. This arises from the fact that in this regime, both determine the duration of the planetary perturbation  $\Delta t_p$  (Gaudi & Gould 1997b). Similarly, there exists a degeneracy between major image ( $d > 1$ ) planetary caustic perturbations and a certain class of binary-source events, namely those with extreme flux ratio between the two sources. For such binary sources, it is always possible to find a binary-source light curve that can exactly reproduce a given set of observables  $t_{0,p}$ ,  $\Delta t_p$ , and  $\delta_p$  (Gaudi 1998). In both cases, the degeneracies can be resolved by accurate and dense photometry.

Next consider high-magnification events (**Figure 5g,h,i**). For such events, the source approaches very close to the lens, creating large, highly distorted images that sweep past the angular Einstein ring during a time  $\sim \Delta t_{FWHM}$  centered on the peak, probing nearly the entire circumference of the ring during this time. Relatively distant planetary companions to the primary, or indeed any companion to the lens, will create a gravitational shear at the position of the primary,

which results in a subtle distortion of the Einstein ring shape, and this can be detected as the highly magnified images sweep by the ring. This is the origin of the central caustic in wide topology planetary lenses  $s > s_w$ . Similarly, relatively close planetary companions (or any close companion) to the primary will create a quadrupole moment, which results in a distortion of the Einstein ring and gives rise to the central caustic in close topology planetary lenses with  $s < s_c$ . For  $q \ll 1$ , the distortion due to the shear of the distant companion and the quadrupole due to the close companion are the same for  $s \leftrightarrow s^{-1}$  (Dominik 1999).

Of course, a planet located close to the Einstein ring can perturb the highly magnified images directly in moderate- to high-magnification events (**Figure 5d,e,f**). This is the origin of the caustics of, and perturbations from, resonant planets with  $d_c < d < d_w$ . Because these images are highly magnified, the range of planet locations relative to the image position that lead to a significant perturbation is large, resulting in a large caustic.

## 2.5. Optical Depth and Event Rate

Microlensing events result from the chance, precise alignment between a foreground lens and background source star and are, thus, unpredictable and rare phenomena. These facts of life strongly influence the practical requirements and implementation of microlensing surveys, and so are fundamental to an understanding of how microlensing planet surveys work. In order to quantify the rarity of microlensing events, in this section we introduce the concepts of the lensing optical depth and event rate, following closely the discussions by Paczyński (1996) and Mao (2008).

The probability that any given star is being significantly lensed at any given time by a foreground compact object (i.e., a lensing star) is typically referred to as the lensing optical depth  $\tau$ . Defining a significantly lensed source as one that has an angular separation from a foreground lens that is less than or equal to the angular Einstein ring radius of the lens (i.e.,  $\beta \leq \theta_E$  and, thus,  $A \gtrsim 1.34$ ), then the optical depth is just the fraction of a given patch of sky with solid angle  $\Omega$  that is covered by the Einstein rings of all foreground lenses. The volume of a shell at a distance  $D_l$  with thickness  $dD_l$  and solid angle  $\Omega$  is  $\Omega D_l^2 dD_l$ , and thus the number of lenses in this shell is  $n(D_l) \Omega D_l^2 dD_l$ , where  $n$  is the number density of lenses. Assuming all lenses have an angular Einstein ring radius  $\theta_E$ , the contribution of the shell to the optical depth is therefore the number of lenses times  $\pi \theta_E^2$ . Integrating along the line of sight,

$$\tau = \frac{1}{\Omega} \int_0^{D_s} n(D_l) \Omega D_l^2 \pi \theta_E^2 dD_l = \int_0^{D_s} n(D_l) D_l^2 \pi \theta_E^2 dD_l. \quad (25)$$

The mass density of lenses of mass  $M$  is related to the number density by  $n = \rho/M$ , but also  $\pi \theta_E^2 \propto M$ , and thus the mass of the lenses drops out of the expression for the optical depth. Although we derived this result assuming a single mass for the lenses, this is also true for a general distribution of masses. Thus, the optical depth depends only on the mass density along the line of sight and not on the mass function of lenses. Inserting the expression for the angular Einstein ring radius, and scaling the distance along the line of sight to the distance to the source, we arrive at a relatively simple expression for the optical depth,

$$\tau = \frac{4\pi G D_s^2}{c^2} \int_0^1 \rho(x) x(1-x) dx. \quad (26)$$

This assumes all the sources are at a fixed distance of  $D_s$ . In fact, sources should be distributed along the line of sight, and thus a more correct derivation must integrate over the source distances as well, weighting by the density of sources (see Kiraga & Paczyński 1994). Consider a crude model for the Milky Way as a spherical, self-gravitating system of lenses centered at the

---

**Lensing optical depth:** the probability that any given star will have a foreground mass aligned within the Einstein ring radius  $\theta_E$  and, thus, will be significantly lensed by it; also equal to the fraction of the sky in a given area covered by such Einstein rings

---

Galactic center with uniform density  $\rho_0$  with total mass  $M_0$  interior to the solar circle. The circular velocity at the solar circle is  $V^2 = GM_0/D_s$ , and the density is  $\rho_0 = 3M_0/(4\pi R_s^3)$ . Integrating Equation 26 and adopting these definitions, we can then write the optical depth as

$$\tau = \frac{2\pi G\rho_0 D_s^2}{3c^2} = \frac{GM_0}{2c^2 D_s} = \frac{V^2}{2c^2}. \quad (27)$$

For  $V = 220 \text{ km s}^{-1}$ , this yields  $\tau \simeq 2.7 \times 10^{-7}$ . The true optical depth toward the Galactic center is  $\sim 3$ – $10$  times larger (Afonso et al. 2003, Popowski et al. 2005, Sumi et al. 2006) because of the flattened nature of the disk and the bar in the Galactic Bulge. See, e.g., Kiraga & Paczyński (1994) and Han & Gould (1995) for theoretical estimates of the optical depth toward the Galactic Bulge and Afonso et al. (2003), Popowski et al. (2005), and Sumi et al. (2006) for observational determinations.

Of somewhat more interest is the microlensing event rate  $\Gamma$ , the rate at which a given background star undergoes a microlensing event due to a foreground lens. If we assume that the foreground lens must come within a minimum angular separation of  $\theta_E$  of the background source to create a detectable microlensing event, then the probability that a given source will exhibit an event in a time  $dt$  is just the fraction of the sky covered by the solid angle of width  $2\theta_E$  and length  $\mu_{\text{rel}} dt$ , integrated over all the lenses along the line of sight. Here  $\mu_{\text{rel}}$  is the proper motion of the foreground lens relative to the source. If we assume that all the events have the timescale  $t_E$ , then a crude estimate of the event rate can be derived in analogy to the derivation for the optical depth,

$$\Gamma dt = \frac{1}{\Omega} \int_0^{D_s} n(D_l) \mu_{\text{rel}} dt \Omega D_l^2 2\theta_E dD_l = \frac{2}{\pi} \frac{dt}{t_E} \left[ \int_0^{D_s} n(D_l) D_l^2 \pi \theta_E^2 dD_l \right], \quad (28)$$

where we have used the identity  $\mu_{\text{rel}} = \theta_E/t_E$ . The integral term in brackets is just the expression for the optical depth derived above (Equation 25), and thus in this approximation,

$$\Gamma = \frac{2}{\pi} \frac{\tau}{t_E}. \quad (29)$$

The median timescale for an event toward the Galactic Bulge is  $\sim 20$  days, and thus  $\Gamma \sim 10^{-5} \text{ year}^{-1} (\tau/10^{-6})$ . In fact, a proper determination of the event rate must not only account for the density distribution of lenses along the line of sight, but also the velocity distributions of the lenses and sources, and density distribution of sources. The distributions of lens and source distances, and lens and source velocity distributions together determine the distribution of lens-source relative proper motions  $\mu_{\text{rel}}$ . Also, whereas the optical depth depends only on the mass density along the line of sight, and not on the mass function of lenses, the event rate depends explicitly on the mass function of lenses. This can be seen from examination of the integrand in the middle equality in Equation 28, where the contribution of the event rate from a range of lens distances  $dD_l$  is  $\propto n\theta_E \propto nM^{1/2} \propto \rho M^{-1/2}$ . Thus, the calculation of the event rate must also integrate over an assumed mass function of lenses. See, e.g., Griest (1991) and Kiraga & Paczyński (1994) for examples of more sophisticated evaluations of the expected event rate for specific models.

The microlensing event rate per star is quite low and, thus, a large number of sources must be monitored in order to detect many microlensing events. For example, OGLE (Optical Gravitational Lens Experiment) currently monitors and analyzes  $\sim 2.5 \times 10^8$  sources in  $\sim 80$  square degrees distributed over 58 individual fields, from which they alert  $\sim 1,500$  events during the  $\sim 8$  month season when the Galactic Bulge is visible (see <http://ogle.astrouw.edu.pl/ogle4/ews/ews.html>).

The event rate distribution as a function of timescale  $t_E$  is quite broad. Recall that the timescale depends on the angular Einstein ring radius and relative source-lens proper motion, which in turn depend on the lens mass and lens and source distances, and the projected velocities of the lens,

source, and observer. Although the source distances generally span a relatively narrow range of a few kiloparsecs centered near the Galactic center, lens distances can range from a few hundred parsecs to the source distance. Similarly, the distributions of lens and source velocities are quite broad and, in particular, stars in the Galactic Bulge have a velocity dispersion of  $\sim 100 \text{ km s}^{-1}$  (Howard et al. 2008). Projection effects further broaden the distribution of relative proper motions. Finally, the distribution of lens masses is itself quite broad, likely spanning at least four orders of magnitude in mass, including free-floating planets, brown dwarfs, stars, and stellar remnants.

**Figure 3b** shows the observed distribution of microlensing event timescales toward the Galactic Bulge, based on observations obtained by the Microlensing Observations in Astrophysics collaboration during 2006–2007 (Sumi et al. 2011). The broad distribution of event timescales is quite apparent. Note that this distribution has not been corrected for the detection efficiency as a function of  $t_E$ ; such a correction would further broaden the distribution. Also shown is a decomposition of the timescale distribution into the contribution of lenses of different ranges of masses, using a model similar to that adopted by Gould (2000a). Clearly the event timescale serves a poor proxy for the lens mass for any individual event. This is because, even at fixed lens mass  $M$  and source distance  $D_s$ , the large range of lens distances and lens and source relative velocities results in a large range of timescales. The distribution of event timescales is generically expected to exhibit asymptotic power-law tails of the form  $d\Gamma/dt_E \propto t_E^3$  for small  $t_E$  and  $\propto t_E^{-3}$  for large  $t_E$  (Mao & Paczyński 1996). The short timescale tail arises from events in which the lens is close to the observer or source, and the long timescale tail arises from events in which the projected velocity between the lens and source is small. These tails can be seen in the distribution of timescales shown in **Figure 3**, although the form for both are distorted by the detection efficiency, which strongly declines for  $t_E \gtrsim 200$  days and declines more gently for  $t_E \lesssim 10$  days. The additional feature in the timescale distribution near  $t_E \sim 2$  days does not conform to this asymptotic tail and strongly suggests a feature in the underlying mass function due to isolated planetary-mass objects (Sumi et al. 2011). We discuss this result in more detail in Section 6.

## 2.6. Advantages and Challenges of the Method

The microlensing method of finding planets has some unique advantages that make it an important component of the complement of planet detection methods at our disposal. However, the method also comes with a unique set of drawbacks, difficulties, and challenges. Both the advantages and disadvantages of the method derive from the basic way in which the method works, namely that planet detection relies on the direct perturbation of images by the gravitational field of the planet, rather than on light from the planet or the indirect effect of the planet on the parent star.

**2.6.1. Advantages and opportunities.** We first discuss the advantages of the microlensing method, focusing in particular on the regions of parameter space to which it is uniquely or particularly sensitive. These include peak sensitivity beyond the snow line, sensitivity to low-mass planets, sensitivity to long-period and/or free-floating planets, sensitivity to a wide range of host stars over a wide range of Galactocentric distances, and sensitivity to multiple-planet systems.

**2.6.1.1. Peak sensitivity beyond the snow line.** Planets are detected concurrently with the lensing events due to their host star when they perturb the images created by a primary lens. Because these images are always located near the Einstein ring when the primary is significantly magnified (see, e.g., **Figure 5**), the planet detection probability is maximized for planets with projected separation  $\sim r_E = D_l \theta_E$ . For a solar mass lens at  $D_l = 4 \text{ kpc}$ , and a source at  $D_s = 8 \text{ kpc}$ , the Einstein ring radius  $r_E \simeq 4 \text{ AU}$  is fortuitously close to Jupiter’s semimajor axis of  $5.2 \text{ AU}$ . More generally, as

originally pointed out by Gould & Loeb (1992), the Einstein ring radius is expected to be located just beyond the region of the protoplanetary disk, where the midplane disk temperature is below the sublimation temperature of water, the so-called snow line. The location of snow line  $a_{sl}$  plays an important role in bottom-up theories of planet formation, as the surface density of solids is expected to increase by a factor of several just beyond the snow line, and thus the timescale to grow a protoplanetary core to a given mass is generically expected to be smallest there as well. The core-accretion theory, in particular, predicts that for typical disk masses, gas giants can only form (just) beyond the snow line (e.g., Lissauer 1987).

Predicting the location of the snow line in a protoplanetary disk and, in particular, how this location should scale with host star mass, is difficult [see Lecar et al. (2006); Kennedy, Kenyon & Bromley (2007); and Kennedy & Kenyon (2008) for discussions]. Evidence based on the composition of main-belt asteroids suggests the snow line in the Solar System was close to  $a_{sl, M_\odot} \sim 2.7$  AU (Abe et al. 2000, Rivkin et al. 2002). If we adopt a linear scaling with host star mass  $a_{sl} = 2.7 \text{ AU}(M/M_\odot)$  (Kennedy & Kenyon 2008) and account for the median projection factor such that  $a_{sl, \perp} = 0.866 a_{sl}$ , then the dimensionless projected separation corresponding to the snow line is

$$s_{sl} \equiv \frac{a_{sl, \perp}}{r_E} \simeq 0.41 \left( \frac{M}{0.5 M_\odot} \right)^{1/2} \left( \frac{D_s}{8 \text{ kpc}} \right)^{-1/2} \left[ \frac{x(1-x)}{0.25} \right]^{-1/2}. \quad (30)$$

Thus, microlensing is intrinsically sensitive to planets at roughly 2–3 times the snow line. This is generally complementary to other techniques, such as radial velocity and transits, which are more sensitive to planets close to their parent stars (**Figure 6**).

In contrast, microlensing is substantially less sensitive to planets in the habitable zones of their parent stars. Assuming the habitable zone is centered at a semimajor axis of  $a_{bz} = \text{AU}(L/L_\odot)^{1/2}$ , and assuming the same projection factor, then we can write the dimensional projected separation of the snow line as

$$s_{bz} \equiv \frac{a_{bz, \perp}}{r_E} = 0.05 \left( \frac{M}{0.5 M_\odot} \right)^2 \left( \frac{D_s}{8 \text{ kpc}} \right)^{-1/2} \left[ \frac{x(1-x)}{0.25} \right]^{-1/2}, \quad (31)$$

where we have assumed  $L/L_\odot = (M/M_\odot)^5$ . Thus, for typical microlensing host star masses and distances, the habitable zone is well inside the Einstein ring radius (Di Stefano 1999). Because planets with projected separation much smaller than the Einstein ring can only be detected by perturbing minor images located very close to the primary lens, whose magnifications are always substantially smaller than unity (see Equation 14), the resulting magnitudes of the planetary perturbations are small and difficult to detect. Furthermore, minor image perturbations are more strongly suppressed in the presence of finite source effects (see Bennett & Rhie 1996 and Gould & Gauchetel 1997). However, from Equation 31, more massive lenses, as well as nearby lenses [Di Stefano 2008; R. Di Stefano & C. Night, unpublished (arXiv:0801.1510)], are more sensitive to habitable planets.

**2.6.1.2. Sensitivity to low-mass planets.** For a point source, the magnitude of the perturbation due to a planet does not depend on the mass of the planet, but rather it depends primarily on the proximity of the source to the caustics created by the planet. Thus, very large perturbations of tens to hundreds of percent are possible for sources that pass very close to or cross these caustics. The cross section of the caustics does depend on the planet mass; for example, the sizes of the planetary caustics scale as the angular Einstein ring radius of the planet and, thus, are  $\propto m_p^{1/2}$ . The detection probability and perturbation durations scale similarly. In other words, planetary deviations get rarer and briefer as the mass of the planet decreases, but the amplitudes can be arbitrarily large for point sources. Finite source effects start to become significant when the cross section of the planetary perturbation region becomes comparable to the angular size of the source,  $\theta_{E,p} \sim \theta_*$ .

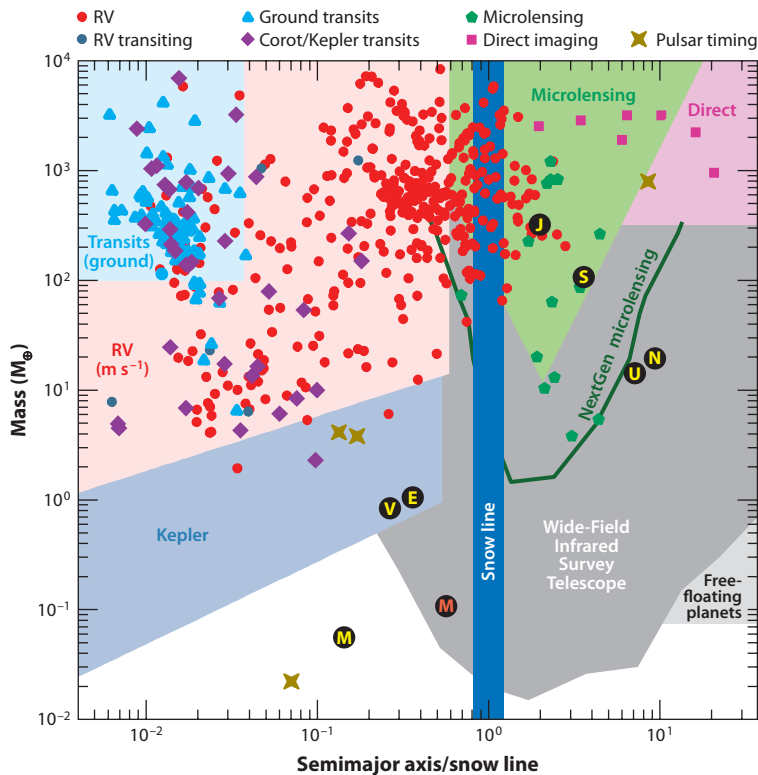


**Figure 6**

Mass versus semimajor axis scaled to the location of the snow line for known exoplanets. Radial velocity (RV) detections are indicated by red circles (*blue* for those also known to be transiting), transit detections are indicated by light blue triangles if detected from the ground and as purple diamonds if detected from space, microlensing detections are indicated by green pentagons, direct detections are indicated by magenta squares, and detections from pulsar timing are indicated by yellow stars. The letters indicate the locations of the Solar System planets. The blue vertical bar designates the snow line, which we have assumed to be located at  $a_{sl} = 2.7 \text{ AU } (M/M_{\odot})$ . For the pulsar planets, we have assumed an arbitrary host star mass of  $1 M_{\odot}$ . The shaded regions show illustrative estimates of the planet discovery space for various methods and experiments. This figure highlights the complementarity of the various planet detection techniques: Transit and radial velocity surveys are generally sensitive to planets interior to the snow line, whereas microlensing and direct imaging surveys are sensitive to more distant planets beyond the snow line.

or  $\rho \sim q^{1/2}$ . For clump giant sources in the Bulge, finite source effects inhibit the detection of planets with mass  $\lesssim 5 M_{\oplus}$  (Bennett & Rhie 1996). For main-sequence sources ( $R \sim R_{\odot}$ ), finite source effects become important for planets with the mass of Earth, but do not completely render them undetectable until masses of  $\sim 0.02 M_{\oplus} \sim 2 M_{\text{Moon}}$  for main-sequence sources (Bennett & Rhie 1996, Han et al. 2005). Thus, microlensing is sensitive to Mars mass planets and even planets a few times the mass of the Moon, for sufficiently small source sizes.

**2.6.1.3. Sensitivity to long-period and free-floating planets.** Microlensing is most sensitive to planets with projected (angular) separations at the time of the primary event that are close to  $\theta_E$ . Planets with separations substantially smaller than this are difficult to detect because the magnifications of the images that are being perturbed are quite small. However, planets with separation



considerably larger than  $\theta_E$  can be detected more readily. This is because the magnification of the major image (outside the Einstein ring) asymptotes to unity for larger separations, as opposed to zero for the minor image. Thus, although the probability of detecting a planet decreases for increasing separations because of the decreasing magnification of the major image, it does not drop to zero even for arbitrarily large separations. For events in which the primary star is also detected, the detection probability for very wide planets with  $s \gg 1$  is  $\sim (\theta_{E,p}/\theta_E)s^{-1} = q^{1/2}s^{-1}$  (Di Stefano & Scalzo 1999b). Of course, it is not required to detect the host star event, and thus very wide or even free-floating planets can be detected when they give rise to apparently isolated, short timescale microlensing events (Di Stefano & Scalzo 1999a, Han et al. 2005).

**2.6.1.4. Sensitivity to planets orbiting a wide range of host stars.** Figure 3b shows a theoretical estimate of the event rate distribution as a function of lens mass from Gould (2000a), which is  $d\Gamma/dM \propto n(M)M^{1/2}$  (see Equation 28). The potential hosts around which one can search for planets span a broad range of masses and include stellar and substellar hosts from brown dwarfs to the Bulge turn-off mass ( $\sim 1M_\odot$ ) and remnants including white dwarfs, neutron stars, and black holes. The slope of the mass function in the stellar regime for  $M \lesssim M_\odot$  is such that roughly equal numbers of hosts are probed per logarithmic interval in mass. Of course, foreground disk stars with mass  $\gtrsim M_\odot$  exist and can also serve as lenses, although they are relatively rare. The distribution of low-mass objects in Figure 3 is arbitrarily cut off at a lower mass limit of  $0.03 M_\odot$ , but could be well extended lower and, indeed, there is evidence for this, as mentioned above (Sumi et al. 2011). Finally, event rates are higher for populations with high velocity dispersions (and, thus, high relative lens-source proper motions), and so thick disk and halo star lenses are overrepresented relative to their number density distributions.

**2.6.1.5. Sensitivity to planets throughout the galaxy.** The microlensing event rate as a function of the lens distance along the line of sight  $D_l$  is proportional to the mass density of lenses at a given distance, weighted by the volume element, relative lens-source proper motion, and Einstein ring radius (see Equation 28). For a fixed lens mass and source distance, and assuming that the relative proper motion is roughly independent of distance, the distribution of lens distances is  $d\Gamma/dD_l \propto \rho(D_l)D_l^{3/2}(1 - D_l)$ . Thus, stars with distances very close to the Earth or very close to the source are less likely to give rise to microlensing events, but otherwise the distribution of lens distances is quite broad, and the event rate remains substantial for lens distances in the range  $D_l \sim 1 - 8$  kpc. Roughly 40% and 60% of microlensing events toward the Bulge are expected to be due to lenses in the disk and Bulge, respectively (Kiraga & Paczyński 1994). This provides the opportunity to determine the Galactic radial distribution of exoplanets, and in particular compare the demographics of planets orbiting two very different populations of stars (the disk and Bulge).

**2.6.1.6. Sensitivity to multiple-planet systems.** Recall that there are essentially three different channels for detecting bound planets concurrently with the host stellar event: in low-magnification events when the source probes the planetary caustic, in high-magnification events when the source probes the central caustic, and in moderate- to high-magnification events when the source probes a resonant caustic. If a host star happens to have multiple planetary companions with projected separations relatively close to the Einstein ring radius, the caustic structure of this triple-lens system can be roughly approximated as the superposition of the caustics of the individual planets (Han 2005) for most combinations of parameters. As a result, if the two planets have separations corresponding to either the close or wide topology, then there will be two sets of planetary caustics corresponding to each planet and two sets of central caustics. The planetary caustics



will generally have random orientations with respect to each other. Thus, for low-magnification events, multiple planets in the same system can be detected only if the source crosses the planetary caustics of both planets or equivalently only if both planets happen to have projected positions sufficiently close to the paths of the two images created by the primary lens. The probability of detecting both planets is thus roughly the product of the individual probabilities, which is typically  $\mathcal{O}(1\%)$  or less (Han & Park 2002). However, the central or resonant caustics are always located near the primary lens and, therefore, in high-magnification events individual planets are detected with near-unity probability regardless of the orientation of the planet with respect to the source trajectory (Griest & Safizadeh 1998), immediately implying that all planets sufficiently close to the Einstein ring radius will have near-unity detection probability (Gaudi, Naber & Sackett 1998). This, along with the fact that high-magnification events are potentially sensitive to very low-mass planets, makes such events excellent probes of planetary systems.

**2.6.2. Weaknesses and challenges.** The unique way in which microlensing detects planets leads to a number of associated challenges. The requirements for overcoming these challenges have largely dictated the practical realization and evolution of microlensing surveys. These challenges include the rare and stochastic nature of microlensing events and difficulties with obtaining detailed information about the detected planets and their hosts.

**2.6.2.1. Rare, unpredictable, and transient signals.** The most important and influential fact of life of gravitational microlensing is that microlensing events require extremely precise, chance alignments between stars that do not repeat. These attributes dictate the nature and practical requirements of microlensing surveys, and we devote Section 3 to a discussion of these issues. The fact that microlensing events do not repeat, combined with the fact that planets detected by microlensing are generally difficult or impossible to confirm using other methods, generally places a higher burden of evidence on the detection of planets with microlensing. In particular, real-time reduction of data in order to enable additional and/or more intensive observations, redundant observations from multiple sites, careful analysis of systematic errors, development of independent checks on model fits, and more stringent detection criteria, are all utilized to avoid ambiguous detections and false positives.

**2.6.2.2. Faint and distant hosts.** Because most microlens hosts are low-mass stars at distances of greater than a kiloparsec, they are typically quite faint (i.e.,  $V \gtrsim 18$ ). Furthermore, their light is typically blended with that from the source and unrelated stars in ground-based seeing. Even if the light from the host star can be isolated, its faintness makes all but the most rudimentary characterization (i.e., determination of its magnitude and color) difficult. In particular, spectra are out of reach for all except the very brightest host stars with current technology. For this reason, and because the radial velocity signals are typically quite small for the long period and/or low-mass planets to which microlensing is sensitive, radial velocity confirmation of microlensing-detected planets is unlikely in the near future.

**2.6.2.3. Limited information about the host and planet.** A generic single lens microlensing event yields only one parameter that depends on the physical properties of the lens star, namely the timescale  $t_E$ , which depends on the mass and distance to the lens, the distance to the source, and the relative lens-source proper motion. Because of the broad range of lens distances and relative lens-source proper motions, the timescale is a poor indication of the lens mass (see **Figure 3**). This unfortunate fact is obviously exacerbated by the fact that the lenses are typically faint. Planetary microlensing perturbations detected in conjunction with the primary event

routinely yield a measurement of the mass ratio  $q$  between the planet and host star, and the instantaneous projected separation  $s$  of the planet at the time of the event in units of  $\theta_E$ . Although  $q$  is of some interest,  $s$  is only weakly correlated with the semimajor axis of the orbit and places essentially no constraint on its eccentricity or orientation. For isolated events due to free-floating or wide-separation planets,  $q$  and  $s$  are not measured; in this case, the only generic constraint on the mass arises from the timescale itself.

As described in detail in Section 4, with some effort, it is possible to extract considerably more information about the host stars and planetary systems detected by microlensing using a combination of constraints from second-order effects during the microlensing events themselves and follow-up observations. With most proposed realizations of a space-based microlensing planet survey, some of these additional constraints are obtained routinely and automatically for the majority of events, enabling robust and reasonably accurate ( $\lesssim 20\%$ ) estimates of the masses of the hosts and planets. Thus, this weakness of the microlensing method would be mostly ameliorated in such surveys.

### 3. PRACTICAL REQUIREMENTS AND MODES OF SEARCHES

The stochasticity of microlensing events requires continuous monitoring with a cadence that is substantially shorter than the timescale of interest. Although the primary microlensing events have a median timescale of  $\sim 20$  days, planetary perturbations to these events last a few days or less. Therefore, even though detecting the primary events only requires cadences of a few days, detecting and accurately characterizing the planetary perturbations to these events requires a relatively high cadence of tens of minutes or less. Because this cadence is less than a day, longitudinally spaced observatories are needed to obtain continuous coverage. However, although  $\sim 10^8$  stars must be monitored to detect the primary events, only the much smaller subsample of stars undergoing microlensing events at any given time must be monitored to detect the planetary perturbations. This smaller sample can be monitored with narrow-angle telescopes.

If there is one free-floating planet of mass ratio  $q$  for every star in the Galaxy or, alternatively, if every star hosts a wide separation planet with mass ratio  $q$ , then the event rate  $\Gamma_p$  of isolated short timescale events due to this population is  $\Gamma_p = q^{1/2} \Gamma_*$ , where  $\Gamma_*$  is the stellar event rate. Thus,  $\Gamma_p \sim 4 \times 10^{-7}$  for the mass ratio between a Jupiter-mass planet and a typical  $0.5\text{-}M_\odot$  stellar microlens, and  $\Gamma_p \sim 2 \times 10^{-8}$  for an Earth-mass planet. Therefore, detecting a few to tens of isolated events due to free-floating or wide planets requires monitoring  $\sim 10^8$  stars continuously with cadences of tens of minutes to a few hours, depending on the planet mass.

The manner in which the above requirements are met depends on the properties of the observing system that is available, most importantly the telescope collecting area and the field of view. In principle, these two properties can be traded off of each other; larger apertures allow one to achieve a given photometric precision on fainter stars and, thus, monitor the same number of stars to a given signal-to-noise ratio over a smaller area. However, the magnitude distribution of stars in the Bulge is relatively flat in the regime of interest. Furthermore, for ground-based seeing, the crowded conditions make achieving photon-limited photometry on fainter stars difficult. Finally, practical and design considerations limit the apertures of telescopes that can be equipped with large field-of-view (FOV) detectors and are available for dedicated use. Thus, the primary property that has dictated the modes of ground-based microlensing surveys has been the FOV, with FOVs of greater than roughly one square degree providing a qualitatively new way of performing microlensing surveys. The modes of operations of microlensing surveys are therefore naturally divided into those realized before and after such detectors were readily available.

### 3.1. First Generation: Alert and Follow-Up

Until relatively recently, with some exceptions, the largest format CCD cameras typically had FOVs of  $\sim 0.25$  deg<sup>2</sup> on 1-m-class telescopes. Thus, many pointings were required to cover a sufficient area, and so fields could only be monitored once or twice per night. As a result, initial microlensing planet searches operated using a two-stage process, as advocated by Gould & Loeb (1992). In this mode, survey teams equipped with large FOV cameras monitor many tens of square degrees with cadences of a few observations per day or less. They then reduce their data real-time, and provide alerts of probable microlensing events, typically before the peak of the event. Some subset of those ongoing microlensing events are then monitored on timescales of hours by follow-up teams, with access to narrow-angle telescopes distributed longitudinally throughout the Southern Hemisphere.

Currently, the survey collaborations include Optical Gravitational Lensing Experiment (OGLE; Udalski 2003) and Microlensing Observations in Astrophysics (MOA; Sako et al. 2008), and the follow-up collaborations include the Probing Lensing Anomalies NETwork (PLANET; Albrow et al. 1998), RoboNet (Tsapras et al. 2009), Microlensing Network for the Detection of Small Terrestrial Exoplanets (MiNDSTEP; Dominik et al. 2010), and the Microlensing Follow Up Network ( $\mu$ FUN; Gould et al. 2010).

As described in Section 2.4.2, there are three qualitatively different types of planetary perturbations to primary microlensing events. These correspond to whether the planet perturbation is arising from a source passing close to the central (**Figure 5g,b,i**), resonant (**Figure 5d,e,f**), or planetary caustic(s) (**Figure 5a,b,c**). Although resonant caustics can be quite large, they are only realized over a relatively small range of mass ratio. Therefore, for practical purposes, we focus on perturbations arising from either central or planetary caustics. The observing strategies required to detect these two types of planetary perturbations are distinct and impose quite different burdens on the follow-up teams. For any given planetary system, the planetary caustics are always larger than the central caustic, and thus the majority of planetary perturbations are caused by planetary caustics, so searching for planets via the influence of the planetary caustics is termed the main channel. In contrast, detecting planets via the main channel requires a substantial commitment of resources because the perturbations are unpredictable and, thus, require continuous sampling; furthermore, the detection probability per event is relatively low, so many events must be monitored. However, detecting planets via their central caustic perturbations requires monitoring high-magnification primary events for a short time (typically a few days) near the peak of the event. In this case, the trade-off is that although high-magnification events are rare (a fraction  $\sim 1/A_{\text{max}}$  of events have maximum magnification  $\gtrsim A_{\text{max}}$ ), they are individually very sensitive to planets. The primary challenge with this channel is in identifying high-magnification events in real time.

The decision of which approach is taken depends on the resources to which the individual collaborations have access. For example, the PLANET collaboration has substantial access to 0.6–1.5-m telescopes located in South Africa, Perth, and Tasmania. With these resources, they are able to monitor dozens of events per season and, so, are able to search for planets via the main channel. However, the  $\mu$ FUN collaboration uses a single 1.3-m telescope in Chile to monitor promising alerted events in order to try to identify high-magnification events substantially before peak. When likely high-magnification events are identified, the other telescopes in the collaboration are then engaged to obtain continuous coverage of the light curve during the high-magnification peak. High-magnification events often reach peak magnitudes of  $I \lesssim 15$  and, thus, can be monitored with relatively small-apertures (0.3–0.4 m). This allows amateur astronomers to contribute to the photometric follow-up. Indeed, over half of the members of the  $\mu$  FUN collaboration are amateurs.

### 3.2. Second Generation: Continuous Monitoring with Large Field-of-View Cameras

The transition to the next generation of ground-based microlensing surveys was enabled by the advent of large-format cameras having FOVs of several square degrees. With such large FOVs, it becomes possible to monitor tens of millions of stars every 10–20 min and, so, detect and simultaneously monitor hundreds or thousands of microlensing events per year with the cadence required to detect perturbations due to very low-mass ( $\sim 1 M_{\oplus}$ ) planets. Thus, next-generation searches operate in a very different mode than the original alert/follow-up model. In order to obtain continuous coverage of the primary events and thereby detect as many of the perturbations as possible, several such telescopes are needed, located on 3–4 continents roughly evenly spread in longitude. This next-generation strategy also enables the detection of short timescale microlensing events due to free-floating or wide-separation planets.

In fact, microlensing surveys are currently in the midst of the transition to the next-generation model. This transition began with the MOA collaboration, who upgraded to the dedicated MOA-II telescope in New Zealand, which has a diameter of 1.8 m and a 2.2-deg<sup>2</sup> FOV (Hearnshaw et al. 2006, Sako et al. 2008). In 2010, the OGLE collaboration commenced the OGLE-IV phase with an upgraded 1.4-deg<sup>2</sup> camera on their dedicated 1.3-m telescope on Las Campanas in Chile (Udalski 2009). Finally, the Wise Observatory 1.0-m telescope in Israel has recently been equipped with a 1-deg<sup>2</sup> camera (Gorbikov, Brosch & Afonso 2010). Together, these groups are continuously monitoring  $\sim 8$  deg<sup>2</sup> with cadences of 15–30 min during the Bulge season (Shvartzvald & Maoz 2011).

The full realization of the next-generation mode of microlensing planet surveys will arrive with the completion of the Korean Microlensing Telescope Network (KMTNet). KMTNet is a project fully funded by the Korean government with plans to build three identical 1.6-m telescopes with 4-deg<sup>2</sup> FOV cameras, one each in South Africa, South America, and Australia. First light for the first telescope to be located on Cerro Tololo is scheduled for early 2013, the second telescope at Sutherland for early 2014, and the final telescope in Siding Springs in late 2014.

### 3.3. Third Generation: Wide-Field Near-Infrared Surveys from Space

Space-based microlensing surveys offer yet another qualitatively different way of searching for planets. Weather, seeing, crowded fields, and systematic errors all conspire to make the detection of planets with mass less than Earth exceedingly difficult from the ground, except for very rare high-magnification events (Bennett 2004). As outlined in Bennett & Rhie (2002), a space-based microlensing survey offers several advantages: the main-sequence Bulge sources needed to detect sub-Earth mass planets are resolved from space, the events can be monitored continuously, and it is possible to observe the moderately reddened solar-type and later source stars in the near-IR to improve the photon collection rate. However, perhaps the most significant qualitative difference between space-based microlensing surveys and ground-based surveys, and thus one of the biggest motivating factors driving the development of a space-based mission, is that the high spatial resolution afforded by space allows unambiguous identification of light from the primary (lens) stars and, so, estimates of the primary and planet masses for the majority of the detections (Bennett, Anderson & Gaudi 2007).

The requirements for a space-based microlensing planet survey are relatively modest: an aperture of at least 1 m, a large FOV camera (at least  $\sim 0.5$  deg<sup>2</sup>) with optical or (preferably) near-IR detectors, reasonable image quality of better than  $\sim 0.25$  arcsec, and an orbit for which the Galactic Bulge is visible for a significant fraction of the year. We discuss possible returns of a space-based survey in Section 7.

## 4. CHARACTERIZING THE HOST STARS AND PLANETS

Because most planet search methods require the detection of light from the planet or star, they tend to target nearby stars to search for planetary companions, with distances of tens to hundreds of parsecs. In many cases, a considerable amount of information (e.g., colors, magnitude, proper motion, parallax, surface gravity) is already known about the host stars even before the planetary companions are found, and for those cases in which the host has not been as well studied, the follow-up data needed to characterize the host can be readily obtained. Thus, host star properties are inferred to reasonable precision for most detections. Furthermore, although each method is subject to its own blind spots in terms of the planet parameters that can be inferred, these methods in general allow for reasonable characterization of the detected planets and orbits. Thus, the planetary systems detected by most planet search methods are typically well characterized and can be readily used as empirical constraints on planet formation models.

As we have discussed, microlensing surveys work very differently from most exoplanet surveys in that the host stars are not targeted and are typically faint and blended with other stars. Furthermore, the routine observables in microlensing events provide little detailed information about the host or planet properties beyond the planet/star mass ratio. In principle, this lack of information limits the usefulness of planetary microlensing detections and hampers the ability to place statistical inferences about the frequency of planets from microlensing surveys in the context of similar results obtained from other planet search methods. This limitation was clear even before microlensing planet surveys were initiated, and attempts to overcome this limitation have been a major focus of the field over the past two decades. These efforts have been met with considerable success. It is now clear that, with additional effort, more information about the host/planet systems can typically be gleaned from a combination of detailed analysis of second-order effects in precise microlensing light curves, as well as from follow-up, high angular resolution imaging. We describe these methods below.

### 4.1. Routine Observables for Generic Microlensing Events

For microlensing events due to single, isolated lenses, five parameters can routinely be measured from the photometry alone: the time of maximum magnification  $t_0$ , the impact parameter of the event in units of the Einstein ring radius  $u_0$ , the Einstein timescale  $t_E$ , the flux from the lensed source star  $F_s$ , and the blend flux  $F_b$ . The blend flux contains light from any stars that are unresolved but are not being lensed. For binary and planetary microlensing events, it is also typically possible to measure the mass ratio  $q$  and projected separation in units of  $\theta_E$ ,  $s$ . Both  $q$  and  $s$  are subject to discrete and continuous degeneracies in certain limiting cases. Those relevant for planetary microlensing were mentioned in Section 2.4.2.

### 4.2. Einstein Ring Radius and Proper Motion

The requirement for detecting a planet via microlensing is generally that the source must pass reasonably close to one or more of the caustics produced by the planetary companion. However, this is also essentially the condition for when the magnification of a source of finite angular size begins to deviate significantly from the point-source approximation (see Section 2.3). Thus, for most planetary microlensing events, these finite source deviations can be used to infer the angular size of the source in units of the angular Einstein ring radius,  $\rho \equiv \theta_*/\theta_E$ .

The angular size of the source can be estimated from its intrinsic color and magnitude using empirical color-surface brightness relations determined from angular size measurements of nearby

stars (Kervella et al. 2004). The source flux  $F_s$  is determined by a fit to the microlensing light curve of the form  $F(t) = F_s A(t) + F_b$ , as the variable magnification of the source allows one to deblend the source and blend fluxes. By obtaining nearly simultaneous measurements in two different passbands during the microlensing event, the apparent source color can be determined without reference to the microlensing model by linear regression of the measurements of the variable flux in the two filters. The extinction toward the source can be estimated by comparison to nearby red giant clump stars (Yoo et al. 2004, Bennett et al. 2010), which have a known and essentially constant luminosity and intrinsic color (Paczynski & Stanek 1998).

Thus, for events in which finite source effects are robustly detected and multicolor measurements are taken while the source is magnified, it is possible to measure  $\theta_E$  (Gould 1994a). This partially breaks the timescale degeneracy because

$$\frac{M}{D_{\text{rel}}} = \frac{c^2}{4G} \theta_E^2. \quad (32)$$

The overwhelming majority of sources are expected to be located in the Bulge. Thus, a measurement of  $\theta_E$  essentially provides a relationship between the mass and the distance to the lens.

By combining the measurement of  $\theta_E$  with that of the overall timescale of the event  $t_E$ , the magnitude of the relative lens-source proper motion can also be inferred  $\mu_{\text{rel}} = \theta_E/t_E$ . Note that this is the geocentric relative lens-source proper motion at the time of the event and, thus, includes a contribution due to the motion of Earth relative to the Sun. Translating to the heliocentric frame requires a (typically small) correction that depends on the relative lens-source parallax  $\pi_{\text{rel}}$ .

### 4.3. Light from the Lens

The majority of the main-sequence stellar lenses are sufficiently bright that their flux can be measured to a relative precision of  $\lesssim 10\%$  with moderate-aperture (1–2-m) telescopes and reasonable ( $10^2$ – $10^4$  s) exposure times, provided that the light from the lens can be isolated. The fit to the microlensing light curve gives the flux of the source  $F_s$ , and the blend flux  $F_b$ . At resolutions of  $\sim 1$  arcsec and in the crowded Bulge fields, there are typically several unrelated stars blended with the source star. Therefore, the lens light cannot be uniquely identified based on such data alone. At the higher resolutions of 0.05–0.1 arcsec available from the *Hubble Space Telescope* (HST) or ground-based adaptive optics imaging, essentially all stars unrelated to the source or lens are resolved. Because the source and lens must be aligned to  $\lesssim \theta_E \sim 1$  mas for a microlensing event to occur and the typical relative lens-source proper motions are  $\mu_{\text{rel}} \sim 5$ – $10$  mas year $^{-1}$  for microlensing events toward the Bulge, the lens and source will be blended in images taken within  $\sim 10$  years of the event, even at the resolution of HST. However, because the microlensing fit gives  $F_s$ , the lens flux can be determined by subtracting this flux from the combined unresolved lens+source flux in the high-resolution image, assuming no blended companions to the lens or source (Bennett, Anderson & Gaudi 2007). There are several potential complications to this procedure to determine the lens flux, including the need to align the high-resolution and microlensing event photometric data sets and to account for the very real possibilities of companions to the lens and/or source. These may introduce substantial uncertainties or ambiguities. See Bennett et al. (2008), Dong et al. (2009b), and Gould et al. (2010) for discussions.

A measurement of the flux of the lens in a single passband, along with a model for extinction as a function of distance and a mass-luminosity relationship, yields a mass-distance relationship for the lens (Bennett, Anderson & Gaudi 2007). A measurement of the lens flux in a second passband yields independent estimates of the mass and distance to the lens, given a model for the intrinsic color as a function of mass and the extinction as a function of wavelength and distance.



#### 4.4. Direct Measurement of the Proper Motion

For typical values of  $\mu_{\text{rel}} \sim 5\text{--}10 \text{ mas year}^{-1}$  for microlensing events toward the Galactic Bulge, after a few years, the lens and source are displaced by  $\sim 0.01 \text{ arcsec}$ . For luminous lenses, and using space telescope or adaptive optics imaging, it is possible to measure this relative lens-source proper motion, either by measuring the elongation of the point-spread function or by measuring the difference in the centroid in several filters if the lens and source have significantly different colors (Bennett, Anderson & Gaudi 2007). The proper motion can be combined with the timescale to give the angular Einstein ring radius,  $\theta_E = \mu_{\text{rel}} t_E$ .

In both cases, the flux of the lens must be known because the magnitude of either the point-spread function elongation or the centroid shift depends on the product of the lens flux and  $\mu_{\text{rel}}$ . Conversely, if the magnitude of  $\mu_{\text{rel}}$  is known independently from the measurement of finite source effects in the light curve, then the flux from the lens can be determined. If both the lens flux and  $\mu_{\text{rel}}$  are known independently, these effects can provide important cross-checks that allow one to test for contamination from companions to the lens or source.

---

**Microlens parallax:** the suite of observable effects that may occur when the assumption of cospatial and/or nonaccelerating observers breaks down and allows one to infer the physical size of the Einstein ring projected to the observer's plane

---

#### 4.5. Microlens Parallax

Microlensing parallax effects occur when the assumption of cospatial and/or nonaccelerating observers is no longer valid. In the expression for the angular separation between the lens and source in units of  $\theta_E$  presented in Equation 16, the observer, lens, and source are assumed to be moving with constant velocity. There is also an implicit assumption that the values of  $t_0$ ,  $u_0$ , and  $t_E$  are constant and, thus, that all observers are all cospatial and moving at the same velocity. The breakdown of any of these assumptions is generally termed (microlens) parallax.

Parallax effects manifest in one of three ways: Orbital parallax occurs when the duration of the microlensing event is a significant fraction of a year, and the acceleration of Earth leads to a significant change in the relative lens-source velocity, resulting in a nonuniform and/or nonrectilinear trajectory of the lens relative to the source and giving rise to deviations from the standard Paczyński light curve (Gould 1992). Terrestrial parallax is due to displacements in the Einstein ring arising from differences in the perspectives of observers located at different observatories. These displacements lead to changes in the observed magnifications, particularly for sources that lie very close to a caustic and so are highly magnified (Holz & Wald 1996). Finally, satellite parallax occurs when the observers are separated by a significant fraction of an Einstein ring, for example, if the event is simultaneously observed from Earth and a satellite in a solar orbit. This gives rise to large differences in the magnification as seen from the two observers, even for relatively moderate magnifications (Gould 1994b, Refsdal 1966).

In all three cases, the magnitude of the effect depends on the size of relevant length scale that gives rise to the different or changing perspective (i.e., the projected separation between the observatories, the projected size of Earth's orbit, or the projected separation between the satellite and Earth) relative to  $\tilde{r}_E \equiv D_{\text{rel}}\theta_E$ , the angular Einstein ring radius projected on the plane of the observer (see **Figure 1**). Orbital parallax deviations are generally only significant for events with timescales that are a significant fraction of a year and, so, long as compared to the median timescale of  $\sim 20$  days. Furthermore, the deviations due to orbital parallax are subject to an array of degeneracies, which can hamper the ability to extract unique microlens parallax parameters (see appendix A of Skowron et al. 2011 for a summary and further references). Parallax measurements made from two well-separated observatories may also be subject to several degeneracies. These degeneracies, and methods to ameliorate them, have been studied by a number of researchers (Refsdal 1966; Gould 1994b, 1995, 1999; Bouteux & Gould 1996; Gaudi & Gould 1997a; Dong



et al. 2007). Finally, terrestrial parallax measurements from only two observatories are subject to degeneracies that can be resolved with simultaneous observations from a third observatory that is not colinear with the other two.

A robust measurement of the microlens parallax allows one to partially break the timescale degeneracy because

$$MD_{\text{rel}} = \frac{c^2}{4G} \tilde{r}_E^2, \quad (33)$$

providing, along with an estimate of the distance to the source, a relationship between the mass and the distance to the lens. Note the functional form of this relation is different than that provided by the measurement of  $\theta_E$ .

**4.5.1. Orbital motion of the planet.** Typically, the timescale of binary and planetary microlensing events are a relatively small fraction of the orbital period of the system, and thus the relative positions of the bodies can be considered fixed during the event. However, in some cases, relative orbital motion of the components during the event can give rise to deviations from the light curve expected under the usual static lens assumption (Dominik 1998). For the general case of a binary lens and a Keplerian orbit, an additional five parameters beyond the usual three static-lens parameters ( $q$ ,  $s$ , and  $\alpha$ ) are needed to fully specify the binary orbit and, thus, the light curve (Dominik 1998). These include the mass of the primary lens, the three components of the companion's velocity relative to the primary, and the projection of the separation of the companion along the line of sight in units of  $\theta_E$ . Typically, however, only two additional parameters can be measured: the two components of the velocity of the secondary relative to the primary projected on the sky. These two components can be parameterized by the fractional rate of the change of the projected binary axis  $\gamma_{\parallel} \equiv \dot{s}/s$  and the angular rotation rate of the projected axis of the binary  $\gamma_{\perp} \equiv -\dot{\alpha}$ . The effect of  $\gamma_{\perp}$  is simply to rotate the magnification pattern of the lens on the sky, whereas a finite value of  $\gamma_{\parallel}$  results in a change in the lens mapping itself with time and, thus, a change in the caustic structure and magnification pattern. The introduction of these additional parameters gives rise to new degeneracies with other microlensing parameters, including the orbital parallax, as described by Skowron et al. (2011). If these degeneracies can be broken and the mass of the primary lens can be measured, then under the assumption of a circular orbit, these two components of the projected velocity completely specify the full orbit of the planet (including inclination), up to a twofold degeneracy (Dong et al. 2009b). In some exceptional cases, even higher order effects may place constraints on the final two parameters, thereby allowing constraints on the full Keplerian orbit of the binary, including eccentricity and inclination (Bennett et al. 2010, Skowron et al. 2011).

**4.5.2. Complete solutions.** In many cases, several of the pieces of information described above can be measured in the same event, providing complete or even redundant measurements of the mass, distance, and transverse velocity of the lens. [See Bennett, Anderson & Gaudi (2007) for a review.] For example, a measurement of  $\theta_E$  from finite source effects or from a direct measurement of  $\mu_{\text{rel}}$ , when combined with a measurement of  $\tilde{r}_E$  from microlens parallax, directly yields the lens mass (see **Figure 1**),

$$M = \left( \frac{c^2}{4G} \right) \tilde{r}_E \theta_E, \quad (34)$$

and with an assumption of the distance to the source, the lens distance

$$D_l^{-1} = \frac{\theta_E}{\tilde{r}_E} + D_s^{-1}, \quad (35)$$

as well as the lens transverse velocity (Gould 1996). Note that this is essentially a direct, geometrical measurement of the lens mass and distance.

Alternatively, a measurement of  $\theta_E$ , combined with a measurement of the flux of the lens, can be used to estimate the lens mass and distance (Bennett, Anderson & Gaudi 2007). This method is less direct, as it relies on model-dependent assumptions about the mass-luminosity relation of lenses and the distribution and properties of the extinction along the line of sight.

**4.5.3. Bayesian analysis.** In general, microlensing events are fit, and uncertainties are determined in the space of canonical microlensing parameters (i.e.,  $t_E$ ,  $\rho$ ,  $\pi_E$ ,  $s$ ,  $q$ ), thereby implicitly imposing priors on the distributions of these parameters. However, reasonable choices for the priors for these parameters generally correspond to unrealistic priors on the physical parameters of interest, such as the mass, distance, and proper motion of the lens. Rather, a reasonable choice for the priors in the physical parameters should result in distributions that are proportional to the expected microlensing event rate. Appropriate choices for the priors can be accommodated by multiplying the local probability density of the canonical parameters by the Jacobian of the transformation between the canonical and physical parameters, weighted by the appropriate priors on the physical parameters (Dominik 2006, Batista et al. 2011, Skowron et al. 2011). When a complete solution of the lens properties is possible and the parameters are strongly constrained, the final posterior distribution of the parameters will be largely independent of the priors. More typically, however, a subset of the parameters is poorly constrained or even completely unconstrained. In such cases, the resulting posterior estimates of the lens and planet properties strongly reflect the choice of priors.

A common situation particularly germane to planetary microlensing events arises when only  $t_E$ ,  $q$ ,  $d$ , and  $\theta_E$  (via  $\rho$ ) can be measured from the light curve. In this case, constraints on the mass and distance to the lens (and so mass and projected separation of the planet in physical units) must rely on the priors to resolve the degeneracy between the mass and distance (Dominik 2006, Dong et al. 2006).

## 5. AN ABRIDGED BACKSTORY

Gravitational lensing generally refers to the deflection of light by massive bodies. This idea has a rich history that predates General Relativity, and can be traced as far back as Sir Isaac Newton. Schneider, Ehlers & Falco (1992) provide a thorough recounting of the history of gravitational lensing. Here we are concerned with gravitational microlensing, which is the special case of gravitational lensing in which multiple images are created but have separations of less than a few milliarcseconds and, hence, are unresolved with current capabilities. It appears as though the concept of gravitational microlensing can be attributed to Einstein. In 1936, Einstein published a paper in which he derived the equations of microlensing by a foreground star closely aligned to a background star, describing the appearance of rings and double images and computing the amount by which the background star would be magnified (Einstein 1936). Although there exist earlier published references to such phenomenon (Lodge 1919, Eddington 1920, Chwolson 1924), it seems that Einstein had been thinking about this idea as far back as 1912 (Renn, Sauer & Stachel 1997) and perhaps had even hoped to use the phenomenon to explain the appearance of Nova Geminorum 1912 (Sauer 2008). However, at the time he presented his derivations in 1936, he dismissed the practical significance of the microlensing effect, concluding that “there is no great chance of observing this phenomenon” (Einstein 1936).

Indeed, there is no “great chance” of observing gravitational microlensing. As discussed in Section 2.5, the optical depth to microlensing is of order  $10^{-6}$  toward the Galactic Bulge and is

generally similar or smaller for other lines of sight in our Galaxy or toward nearby galaxies. At least partly due to this low probability, the idea of gravitational microlensing lay mostly dormant for five decades after Einstein's 1936 paper (with some notable exceptions, e.g., Liebes 1964, Refsdal 1964). It was not until the seminal paper by Paczyński (1986) that the idea of gravitational microlensing was resurrected, and then finally put into practice with the inception of several observational searches for microlensing events toward the Large and Small Magellanic Clouds and Galactic Bulge in the early 1990s (Alcock et al. 1993, Aubourg et al. 1993, Udalski et al. 1993). Many thousands of microlensing events have been detected to date, by a number of different collaborations and toward several lines of sight, with the vast majority of events found toward the Galactic Bulge.

Even before the first microlensing events were detected, it was suggested by Mao & Paczyński (1991) that gravitational lensing by binary lenses could give rise to distinctive light curves, provided that the separations of the components were roughly commensurate with the Einstein ring of the total mass of the lens. In particular, they noted the presence of caustics and the appearance of extra pairs of images, as well as sharp changes in the magnification when the source traverses the caustic. They also noted that the angle-averaged cross sections for the source to encounter the caustics in binary lenses remained substantial even for low-mass ratios of  $q \sim 10^{-3}$ , similar to Jupiter and the Sun. They therefore argued that microlensing might be a fruitful way of searching for extrasolar planetary systems, in particular estimating that 5–10% of all microlensing events might exhibit detectable deviations if all lenses hosted Jupiter-mass companions with angular separations within a factor of about three of the Einstein ring.

Gould & Loeb (1992) considered this novel method of detecting planets in considerable detail and laid out the practical requirements for an observational survey for planets with microlensing. Such surveys began in earnest not long after, with the formation in 1995 of several follow-up collaborations dedicated to searching for planetary deviations in ongoing events (Alcock et al. 1996, Albrow et al. 1998, Rhie et al. 2000). These initial searches adopted the basic two-tier survey/alert approach advocated by Gould & Loeb (1992): monitoring ongoing events alerted by survey collaborations (e.g., Udalski et al. 1994, Alcock et al. 1996) and using networks of small telescopes distributed throughout the Southern Hemisphere. Although microlensing planet searches have matured considerably since their initiation, this basic approach is still used to this day, although as described in Section 3.2, microlensing surveys are currently transitioning to a second-generation, survey only mode.

From 1995–2001, no convincing planet detections were made, primarily because the number of events being alerted each year by the survey collaborations was relatively modest ( $\sim 50$ – $100$ ). Thus, there were only a few events ongoing at any given time, and often these were poorly suited for follow-up. In particular, the low rate of events directly translated to a very low rate of high-magnification events, which were, in the meantime, realized to be individually very sensitive to planets (Griest & Safizadeh 1998). Although interesting upper limits were placed on the frequency of Jovian planets (Gaudi et al. 2002; Snodgrass, Horne & Tsapras 2004), perhaps the most important result during this period was the development of the practice of the microlensing method, which resulted in its transformation from a theoretical abstraction to a viable, practical method of searching for planets.

In 2001, the OGLE collaboration (Udalski 2003) upgraded to a new camera with a 16-times larger FOV; they were then able to monitor a larger area of the Bulge with a higher cadence. As a result, in 2002 OGLE began alerting nearly an order of magnitude more events per year than before the upgrade. These improvements in the alert rate and cadence, combined with improved cooperation and coordination between the survey and follow-up collaborations, led to the first discovery of an extrasolar planet with microlensing in 2003 by the MOA and OGLE collaborations

(Bond et al. 2004). The MOA collaboration completed their upgrade to a 1.8-m telescope and 2-deg<sup>2</sup> camera in 2006 (Sako et al. 2008), and by 2007 the OGLE and MOA collaborations were alerting a combined  $\sim 900$  events per year, thus ushering in the first golden age of microlensing planet searches.

## 6. RESULTS: DETECTIONS AND THE DEMOGRAPHICS OF PLANETS BEYOND THE SNOW LINE

To date, the discovery via microlensing surveys of 14 planets in 13 systems have been published (Bond et al. 2004, Udalski et al. 2005, Beaulieu et al. 2006, Gould et al. 2006, Bennett et al. 2008, Gaudi et al. 2008, Dong et al. 2009a, Janczak et al. 2010, Sumi et al. 2010, Batista et al. 2011, Miyake et al. 2011, Muraki et al. 2011, Yee et al. 2012). All of these discoveries have been the result of collaborative efforts between various combinations and permutations of the survey and follow-up teams introduced in Section 3.1. The estimated masses of the microlensing host stars span a relatively wide range from  $\sim 0.08 M_{\odot}$  to  $\sim 0.64 M_{\odot}$ . Similarly there is a substantial range of planet masses from  $\sim 3 M_{\oplus}$  to  $3.5 M_{\text{Jup}}$ . Super-Earths, Neptunes, Saturns, Jupiters, and Super-Jupiters are all represented in the microlensing sample.

**Figure 6** shows the estimated masses and semimajor axes scaled to the location of the snow line for the detected microlensing planets, where we have assumed a snow line location  $a_{sl} = 2.7 \text{ AU} (M/M_{\odot})$  (Kennedy & Kenyon 2008). For comparison, we also show the masses and scaled semimajor axes for exoplanets discovered by the radial velocity, transit, direct detection, and pulsar timing methods, as well as the planets in our Solar System. As expected, most of the planets were detected with projected separations within a factor of about three of the snow line, with a median value of  $\sim 2.6 a_{sl}$ . Rather than review the properties of each of the 14 detections individually, we instead focus on a few systems or groups of detections that are of particular interest and then summarize what has been learned about the demographics of exoplanets based on the ensemble of detections.

### 6.1. Individual Detections of Interest

**6.1.1. Cold super-earths.** OGLE-2005-BLG-390Lb is a very low-mass planet with a planet/star mass ratio of only  $q \sim 8 \times 10^{-5}$  (Beaulieu et al. 2006). A Bayesian analysis combined with a measurement of  $\theta_E$  from finite source effects indicates that the planet likely orbits a low-mass M dwarf with  $M = 0.22^{+0.21}_{-0.11} M_{\odot}$  and, thus, has a mass of only  $5.5^{+5.5}_{-2.7} M_{\oplus}$ . Its separation is  $2.6^{+1.5}_{-0.6} \text{ AU}$  and, so, has a cool equilibrium temperature of  $\sim 50 \text{ K}$ . This planet was the first discovery of a cold super-Earth, a new class of planets inhabiting a region of parameter space that was previously unexplored by any method.

Core-accretion models of giant planet formation generally predict that there should exist a substantial population of such super-Earths with mass  $\leq 15 M_{\oplus}$  immediately beyond the snow line. This scenario generally predicts a protracted phase of evolution at  $\sim 5\text{--}15 M_{\oplus}$ , during which the growth of the planets is expected to be slow (Pollack et al. 1996, Ida & Lin 2004). This phase occurs after the core has accreted the majority of the solid material in its vicinity, but before the gaseous envelope is sufficiently massive to trigger rapid gas accretion. If the disk disperses during this protracted phase, the growth will stall at this mass, resulting in a “failed Jupiter.” Such models also generally predict that these failed Jupiters should be even more common around low-mass stars, as their disk masses are lower and their dynamical times at the locations of planet formation are longer (e.g., Laughlin, Bodenheimer & Adams 2004; Kennedy & Kenyon 2008; Alibert, Mordasini & Benz 2011; but see Kornet, Wolf & Różyczka 2006).

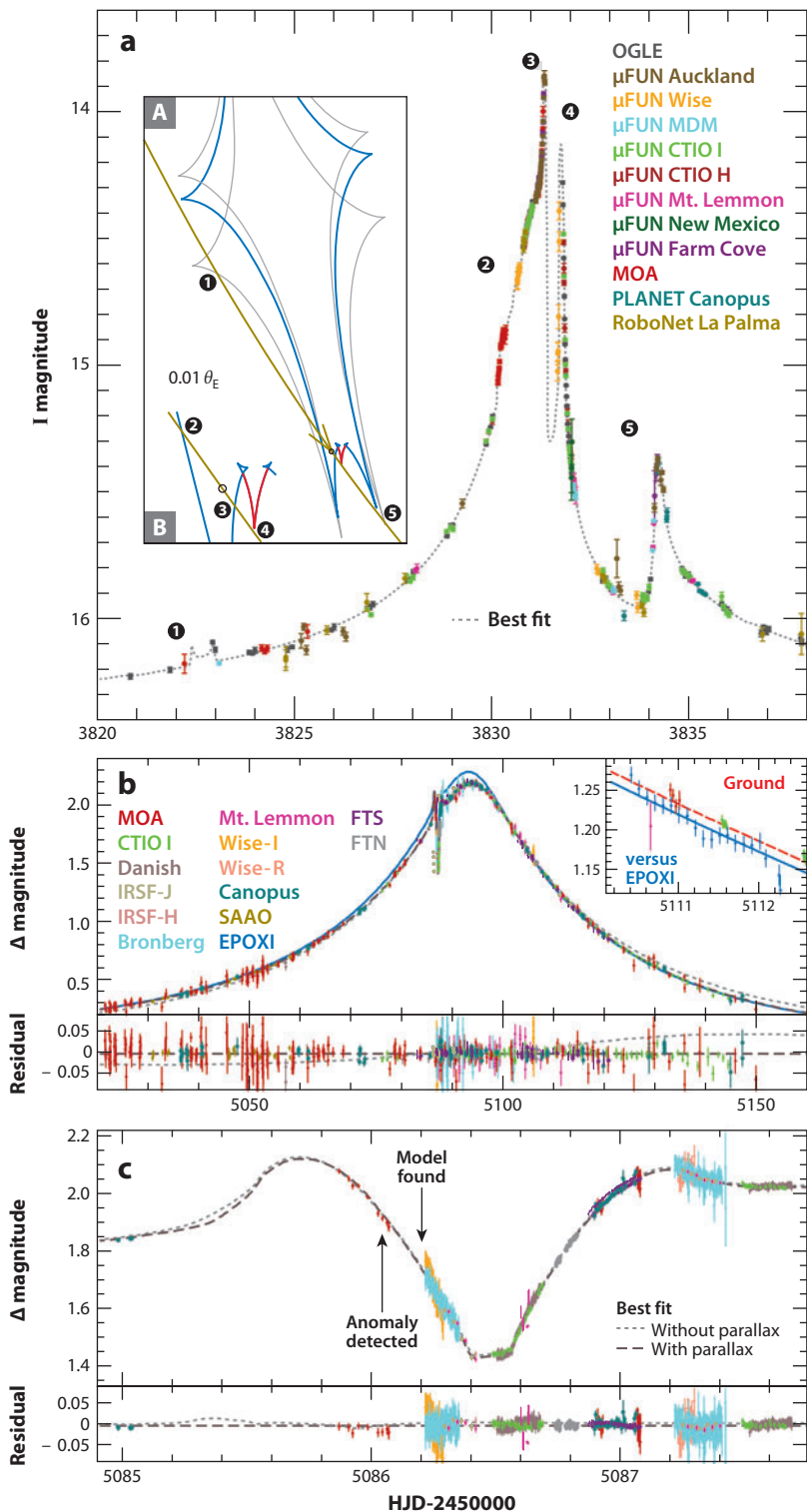
MOA-2007-BLG-192Lb appears to be another member of this class, also being a very low-mass, cool planet likely orbiting a star with a mass near the hydrogen-burning limit (Bennett et al. 2008). The planet/star mass ratio is  $q \sim 10^{-4}$ , about twice that of Neptune and the Sun; however, a combination of constraints from orbital parallax, weak finite source effects, and lens flux detected via adaptive optics imaging constrain the primary to have a mass of only  $M = 0.084^{+0.015}_{-0.012} M_{\odot}$  (Kubas et al. 2012), yielding a planet mass of  $\sim 3.2^{+5.2}_{-1.8} M_{\oplus}$ . Unfortunately, in this case, coverage of the planetary perturbation was sparse, and as a result the planet mass has a substantial uncertainty.

Finally, MOA-2009-BLG-266Lb is the third cold super-Earth discovered via microlensing (Muraki et al. 2011). In contrast to the first two detections, the mass of both the planet and its host star were well-measured in this case. The source star in the MOA-2009-BLG-266 microlensing event was bright, enabling exquisite photometry of the light curve (see **Figure 7**). Furthermore, the planetary perturbation itself was well covered, having been discovered in real-time and monitored by a number of telescopes. As a result, the planetary mass ratio of  $q = 5.63 \pm 0.25 \times 10^{-4}$  has an uncertainty of only  $\sim 4\%$ . Furthermore, both orbital parallax and finite source effects were strongly detected in the light curve, resulting in precise estimates of the host star and planet masses of  $M_* = 0.56 \pm 0.09 M_{\odot}$  and  $m_p = 10.4 \pm 1.7 M_{\oplus}$ , respectively. It is worth noting that the orbital parallax measurement was corroborated by a satellite parallax measurement from observations of the event made with the *EPOXI* spacecraft. Assuming circular orbits and random orientations, the planet's semimajor axis is  $a = 3.2^{+1.9}_{-0.5}$  AU, placing this object at roughly twice the snow line distance. MOA-2009-BLG-266Lb has the mass expected for a core whose growth stalled during the protracted phase of slow gas accretion, and so may be a representative example of such a population.

**6.1.2. Massive companions to M dwarfs.** As mentioned above, the favored core-accretion theory of giant planet formation generally predicts that massive giant planets should be relatively rare around low-mass stars. Therefore, it is interesting to note that 3 of the 14 microlensing planets whose discoveries have been published are likely super-Jupiter companions to M dwarfs. In the case of OGLE-2005-BLG-071Lb (Udalski et al. 2005), this categorization is fairly secure: a combination of HST photometry, finite source effects, and orbital parallax allow for a robust

**Figure 7**

(a) Data and best-fit model of the OGLE-2005-BLG-109 microlensing event, arising from a two-planet system. (*Inset A*) The source trajectory through the caustic created by the two-planet system is shown as the thick dark yellow curve. The shape and orientation of the caustic due to both planets at the peak of the event is shown by the blue and red curves. The five light curve “features” are caused by the source crossing or approaching the caustic; the approximate locations of the features are labeled with circled numbers. The majority of the caustic (in *blue*) is due to only the outer (Saturn-analog) planet; this portion of the caustic explains four of the five features. The portion of the caustic arising from the second (Jupiter-analog) planet is shown in red. This additional cusp in the caustic is required to explain Feature 4 in the light curve; as such, Feature 4 signals the presence of a second (Jupiter-analog) planet. The light gray curves show the caustic at the time of Features 1 and 5. (*Inset B*) A zoom of the source trajectory and caustic near the times of Features 2, 3, and 4. From Gaudi et al. (2008). (*b,c*) Data and best-fit model of the MOA-2009-BLG-266 microlensing event, arising from a cold,  $\sim 10 M_{\oplus}$  planet and an M dwarf host. (*b*) The large upper panel shows 140 days centered on the peak of the primary event with the residuals from the best-fit model in the lower panel, whereas (*c*) the large upper panel shows a close-up of the planetary deviation, with the residuals in the lower panel. In all four panels, the gray dotted curve is the best-fit model without orbital parallax. The inset (in *b*) shows the data of the event taken from the *EPOXI* satellite, which is offset from the ground-based measurements due to the separation between the *EPOXI* satellite and Earth at the time of the observations. From Muraki et al. (2011); reproduced by permission of the AAS.





determination of the primary mass and distance  $M = 0.46 \pm 0.04 M_{\odot}$ , a distance of  $D_l = 3.2 \pm 0.4$  kpc, and a planet mass and projected separation of  $m_p = 3.8 \pm 0.4 M_{\text{Jup}}$  and  $r_{\perp} = 3.6 \pm 0.2$  AU, respectively (Dong et al. 2009a). Furthermore, the primary has thick-disk kinematics with a projected velocity relative to the local standard of rest of  $v = 103 \pm 15$  km s<sup>-1</sup>, suggesting that it may be metal poor. In the case of MOA-2009-BLG-387Lb (Batista et al. 2011), finite source effects and orbital parallax are both strongly detected; however, the orbital parallax signal in this case is highly degenerate with the signal due to the orbital motion of the planet, thus degrading the accuracy of the primary mass and distance measurement. The median and 90% confidence limits on the mass and distance of the host are  $M = 0.19^{+0.30}_{-0.12} M_{\odot}$  and  $D_l = 5.69^{+2.18}_{-2.19}$  kpc, and mass and semimajor axis of the planet are  $m_p = 2.56^{+4.15}_{-1.58} M_{\text{Jup}}$  and  $a = 1.82^{+0.86}_{-0.73}$  AU, respectively. For MOA-2011-BLG-293Lb, only a Bayesian estimate of the lens host mass and distance are available, which yields  $M = 0.44^{+0.27}_{-0.17} M_{\odot}$  and  $D_l = 7.15 \pm 0.65$  kpc, and a planet mass of  $m_p = 2.4^{+1.4}_{-0.9} M_{\text{Jup}}$  (Yee et al. 2012). Thus, although there are substantial uncertainties, these two systems are also likely to be M dwarfs hosting super-Jupiter companions. Although the existence of super-Jupiter companions to M dwarfs is not unexpected, and indeed several have also been detected in radial velocity surveys (e.g., Forveille et al. 2011), the fact that 3 of the 14 planets detected by microlensing fall into this category suggests that they are not uncommon, which may pose a challenge for core-accretion models and, so, may be suggestive of an alternate mode of formation for such massive planetary companions (see also Section 6.2).

**6.1.3. OGLE-2006-BLG-109Lb,c: a jupiter/saturn analog.** OGLE-2006-BLG-109Lb is the first multiplanet system discovered via microlensing (Gaudi et al. 2008, Bennett et al. 2010). As shown in **Figure 7**, the light curve exhibited five distinct deviations from a single lens curve in the span of roughly two weeks. Four of these features are attributable to the source crossing or passing close to the resonant caustic of a Saturn-mass planet, whereas the fifth feature is due to the source approaching the tip of the central caustic of an inner, Jupiter-mass planet. Besides the basic signatures of the two planets, the light curve exhibits finite source effects and orbital parallax, allowing for measurements of the primary mass and distance and, so, planet masses and projected separations. The primary mass measurement is corroborated by a Keck adaptive optics *H*-band image of the target that yields a measurement of the flux of the lens that is consistent with the mass inferred entirely from the microlensing observables.

The OGLE-2006-BLG-109Lb planetary system bears a remarkable similarity to a scaled version of Jupiter and Saturn. The primary is an M dwarf with a mass of  $M = 0.51^{+0.05}_{-0.04} M_{\odot}$  at a distance of  $D_l = 1.51^{+0.11}_{-0.12}$  kpc. The two planets have masses of  $0.73 \pm 0.06 M_{\text{Jup}}$  and  $0.27 \pm 0.02 M_{\text{Jup}}$  and separations of  $2.3 \pm 0.5$  AU and  $4.5^{+2.1}_{-1.0}$  AU, respectively. Thus, the masses of the two planets are very similar to Jupiter and Saturn, as are their semimajor axes when scaled to the location of the snow line.

## 6.2. The Demographics of Exoplanets from Microlensing

As is apparent from **Figure 6**, the planets discovered with microlensing have a roughly uniform distribution in mass from a few Earth masses to a few Jupiter masses and have a distribution in semimajor axis that is centered at  $\sim 2.6 a_{\text{sl}}$ . Because the microlensing detection sensitivity declines with planet mass (ratio) as roughly  $q^{0.3-0.6}$  (Gould et al. 2010, Sumi et al. 2010), the (approximately) uniform distribution in mass implies that the intrinsic frequency of planets at these separations is (approximately) a power law, with the frequency increasing toward low-mass planets.

More quantitative analyses of the implications of the microlensing detections for the demographics of exoplanets beyond the snow line have been performed by a number of researchers. Based on the first two detections of cold, low-mass planets through microlensing, Gould et al.



(2006) estimated that, at 90% confidence,  $38^{+31}_{-22}\%$  of stars host cold super-Earths/Neptunes with separations in the range of 1.6–4.3 AU. By adopting a simple model for the scaling of the detection efficiency with  $q$ , Sumi et al. (2010) used the distribution of mass ratios of the 10 microlensing planets discovered up to that point to derive an intrinsic mass (ratio) function of exoplanets beyond the snow line of  $dN/dq \propto q^{-1.68 \pm 0.20}$ . This implies that cold Neptunes/super-Earths ( $q \sim 5 \times 10^{-5}$ ) are  $7^{+6}_{-3}$  times more common than cold Jupiters ( $q \sim 10^{-3}$ ).

Gould et al. (2010) improved upon previous results by performing a rigorous analysis of a carefully selected, unbiased sample of 13 high-magnification ( $A_{\max} > 200$ ) microlensing events that were densely monitored over their peak during 2005–2008. From the six planets detected, and accounting for the detection sensitivity of all the events in the sample, Gould et al. (2010) estimated the frequency of planets beyond the snow line with mass ratios in the range of  $10^{-4.5} \leq q \leq 10^{-2}$  to be

$$\frac{d^2 N_{\text{pl}}}{d \log q \, d \log s} = (0.36 \pm 0.15) \text{dex}^{-2}. \quad (36)$$

This measurement is centered at  $q = 5 \times 10^{-4}$  and a projected separation  $\sim r_E$ , which corresponds to  $m_p = 83 M_{\oplus} \sim M_{\text{Saturn}}$  and  $\sim 2.5$  AU for the typical host mass of  $\sim 0.5 M_{\odot}$  and typical host distance. **Figure 8** compares this result to planet frequencies determined from radial velocity surveys at different semimajor axes. The frequency of giant (Saturn-mass) planets inferred from microlensing is high, but this is apparently consistent with the extrapolation of the frequency of giant planets orbiting G dwarfs from Cumming et al. (2008) to the region beyond the snow line where microlensing is sensitive, assuming the scaling of planet frequency with distance in units of  $a_{\text{sl}}$  is similar for G and M hosts. However, more comparable M-dwarf radial velocity surveys (Johnson et al. 2010, Bonfils et al. 2012) find a factor of  $\sim 20$ – $30$  times lower normalization for planets with periods of  $\lesssim 1,000$  days. Although the lower intrinsic frequency of relatively short-period giant planets found by Johnson et al. (2010) is a confirmation of the generic prediction of the core-accretion theory of giant planet formation (Laughlin, Bodenheimer & Adams 2004), the much higher frequency found beyond the snow line by Gould et al. (2010) may be difficult to accommodate in the context of this theory.

Gould et al. (2010) also estimated that, if all planetary systems contained analogs of our giant planets with distances scaled by the snow line, then among the 13 events,  $\sim 6$  should have displayed evidence of two or more planets, compared to the single multiple-planet event OGLE-2006-BLG-109, indicating that  $\sim 15\%$  of stars host Solar System analogs.

Cassan et al. (2012) combined the analysis of six years of monitoring of relatively low-magnification ( $A_{\max} \lesssim 50$ ) microlensing events (resulting in three detections), with the mostly independent results from Sumi et al. (2010) and Gould et al. (2010) to estimate a power-law mass function of planets,

$$\frac{d^2 N_{\text{pl}}}{d \log a \, d \log m_p} = 10^{-0.62 \pm 0.22} \left( \frac{m_p}{M_{\text{Saturn}}} \right)^{-0.73 \pm 0.17}. \quad (37)$$

This implies an expectation value of  $\langle N_{\text{pl}} \rangle = 1.6^{+0.7}_{-0.9}$  planets per star in the range of 0.5–10 AU and  $5 M_{\oplus}$ – $10 M_{\text{Jup}}$ .

After their upgrade to a 1.8-m telescope and 2-deg<sup>2</sup> camera in 2006 (Sako et al. 2008), the MOA collaboration began monitoring several tens of fields with cadences of 10–50 min, thus dramatically increasing their efficiency in detecting short-timescale ( $t_e \lesssim 2$  day) events. Sumi et al. (2011) analyzed two years of data from 22 high-cadence MOA fields, identifying 474 microlensing events with the distribution of  $t_E$  shown in **Figure 3**. They find a clear and robust excess of events with  $t_E \sim 1$  day above a power-law or lognormal model for the low-mass end of the stellar/brown

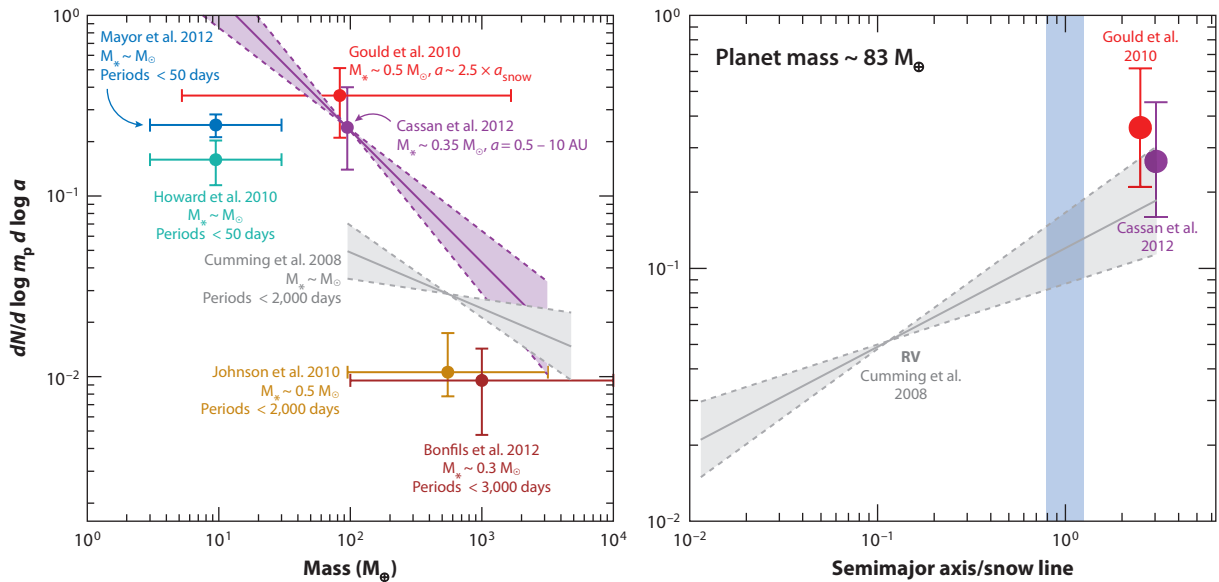


**Figure 8**

(a,b) Planet frequencies determined via microlensing (Gould et al. 2010, Cassan et al. 2012) and radial velocity (RV) (Cumming et al. 2008, Howard et al. 2010, Johnson et al. 2010, Mayor et al. 2012) for different primary masses. (a) Planet frequencies versus planet mass, for various semimajor axis ranges. The Cumming et al. (2008), Mayor et al. (2012), and Howard et al. (2010) RV samples contain primarily  $\sim 1 M_\odot$  hosts. However, the Johnson et al. (2010) and Bonfils et al. (2012) RV samples contain lower mass hosts of  $\sim 0.3\text{--}0.5 M_\odot$  and, thus, can be directly compared to the Gould et al. (2010) and Cassan et al. (2012) microlensing samples. (b) Planet frequencies as a function of semimajor axis in units of the snow line, here assumed to be  $a_{sl} = 2.7 \text{ AU}(M/M_\odot)$  for a host star of mass  $M$ . The Cassan et al. (2012) and Cumming et al. (2008) frequencies have been normalized to the typical planet mass of the Gould et al. (2010) sample of  $\sim 83 M_\oplus$ . For the microlensing frequencies, we have assumed a separation of  $\sim 2.5 (M/0.5 M_\odot)^{-1/2}$  times the snow line, corresponding to the deprojection of the typical Einstein ring radius of a star of mass  $M$ . The mean mass of the Gould et al. (2010) hosts is  $\sim 0.5 M_\odot$ , whereas it is  $\sim 0.35 M_\odot$  for the Cassan et al. (2012) sample. Both panels are adapted from Gould et al. (2010) and reproduced by permission of the AAS.

dwarf mass function, which they interpret as due to a population of unbound or wide-separation Jupiter-mass objects. Sumi et al. (2011) infer this population must be about two times more common than main-sequence stars and suggest that these are likely to be free-floating, rather than bound, based on a comparison with constraints from direct imaging experiments for wide-separation planets.

## 7. THE FUTURE

In the nine Bulge seasons since the first planet discovery using microlensing (2003–2011), 14 planet discoveries have been announced, and another  $\sim 12$  secure planets have been detected that await analysis and/or publication, for an average rate of about three detections per season. In detail, the rate of detections has increased systematically during this period, correlated with the upgrade to MOA-II in 2006, the upgrade to OGLE-IV, and the addition of the Wise Observatory 1-deg<sup>2</sup> camera in 2011.

With the MOA-II, OGLE-IV, and Wise Observatory components in place, microlensing planet surveys are currently in the first phase of the next generation of surveys (or, perhaps, “Generation 1.5”). As mentioned previously, this next-generation model is characterized by

observations with several telescopes spread in longitude and equipped with large FOV cameras, enabling high-cadence, continuous monitoring of a large number of primary events and, thus, simultaneous detection of both the primary events and planetary perturbations, eliminating the need for the alert/follow-up model. Together, these groups are monitoring  $\sim 8 \text{ deg}^2$  with cadences of 15–30 min during the Bulge season and can expect perhaps several dozens of planet detections over the next few years (Shvartzvald & Maoz 2011).

KMTNet will complete the transition to the next generation with its first Bulge season including the entire network scheduled for 2015. KMTNet will provide a significant improvement over the Generation 1.5 survey by having larger apertures and larger FOVs for most longitudes, more continuous access to the Bulge with a telescope in South Africa, and some weather redundancy with a telescope in Australia (versus New Zealand for MOA) and Cerro Tololo (versus Las Campanas for OGLE).

Of course, besides finding more planets, next-generation surveys will also have improved sensitivity to lower-mass, terrestrial planets. Detailed simulations of various realizations of next-generation microlensing surveys have been performed by several groups (B. Gaudi, C. Han, and A. Gould, unpublished; Bennett 2004, Shvartzvald & Maoz 2011). These simulations reach similar conclusions: next-generation surveys will increase the planet detection rate at fixed mass by at least a factor of several over the original alert/follow-up surveys. In particular, if Earth-mass planets with semimajor axes of several astronomical units are common around main-sequence stars, a next-generation microlensing survey should detect several such planets per year.

For reasons summarized in Section 3.3, the true potential of microlensing can ultimately only be realized from space. Interestingly, the requirements for a space-based microlensing planet survey are either very similar to, or less stringent than, the requirements for a number of the proposed dark energy missions, in particular, those that focus on weak lensing measurements, thus making it attractive to consider a combined dark energy/planet finding mission that could be accomplished at a substantial savings compared to doing each mission separately (Gould 2009). Indeed, this argument, combined with the strong individual science cases for a space-based microlensing exoplanet survey, a dark-energy survey, and a general wide-field IR survey, led the 2010 Astronomy and Astrophysics Decadal Survey to recommend just such a joint mission, the Wide-Field InfraRed Survey Telescope (WFIRST, Green et al. 2011) as its top priority for a large space mission. The parameters of the ESA dark energy mission EUCLID also fulfill the requirements for a microlensing survey (Beaulieu et al. 2010).

The potential yields from a space-based microlensing survey with WFIRST, EUCLID, or something similarly capable, are impressive. These missions could, in principle, be sensitive to all planets with mass  $\gtrsim 0.1 M_{\oplus}$  and separations  $a \gtrsim 0.5 \text{ AU}$  (**Figure 6**), including free-floating planets (Bennett & Rhie 2002, Beaulieu et al. 2010, Green et al. 2011). This range includes analogs to all the Solar System planets except Mercury. Assuming a substantial commitment of observing time and reasonable priors on the exoplanet frequency distribution, such surveys could detect several thousands of bound planets, including several hundreds with mass less than  $\sim 10 M_{\oplus}$ , as well as free-floating planets with mass less than the Earth. The survey would also detect a number of habitable Earth-mass planets that is comparable to the number expected from the *Kepler* mission (Borucki et al. 2010), and so would provide an important independent measurement of  $\eta_{\oplus}$ . When combined with complementary surveys (such as *Kepler*), a space-based microlensing planet survey would determine the demographics of free-floating planets and bound planets at arbitrary separations with masses greater than that of Earth orbiting stars with masses less than that of the Sun. Finally, the majority of the microlensing planet detections with main-sequence hosts will have estimates of the masses and distances to the primaries and the masses and physical projected separations of the planets.

In addition to a potentially large increase in the number of planet detections and range of parameter space explored, the future of microlensing will also likely bring additional insights into the general question of how much information can be extracted from individual events. Indeed, the first detections of exoplanets with microlensing have already provided important lessons in this regard. When microlensing planet surveys were first being developed, it was thought that the primary virtue of the method would be solely its ability to provide statistics on large-separation and low-mass planets, and that individual detections would be of little interest because the only routinely measured property of the planets would be the planet/star mass ratio. In fact, experience with modeling of actual events has shown that much more information can typically be gleaned from a combination of a detailed analysis of the light curve, and follow-up, high-resolution imaging (Section 4). It remains an open question of how much more information can, in principle, be gleaned from individual detections, as well as which and what fraction of events are the most likely to yield such precious information.

Finally, the increase in the number of events detected and monitored will yield the detection of rare microlensing exotica. Circumbinary planets, planetary satellites, planetary companions to the source, and systems of more than two planets are all potentially detectable in microlensing surveys. Of course, the most interesting systems will undoubtedly be those that we have not anticipated.

## DISCLOSURE STATEMENT

The author is not aware of any affiliations, memberships, funding, or financial holdings that might be perceived as affecting the objectivity of this review.

## ACKNOWLEDGMENTS

I am privileged to be able to review a field that owes its existence and success to the hard work, dedication, and vision of a few early pioneers, some of whom are no longer with us today. Their perseverance and sheer stubbornness are truly inspiring, particularly given the plethora of practical and social obstacles that had to be overcome to make microlensing surveys a success. I would like to thank all of my collaborators in microlensing over the past 15 years, and I am particularly grateful to A. Gould for fruitful discussions and general guidance. I apologize to those whose work I was unable to discuss due to space limitations. I am delighted to acknowledge support from NASA and the National Science Foundation.

## LITERATURE CITED

- Abe Y, Ohtani E, Okuchi T, Righter K, Drake M. 2000. In *Origin of the Earth and Moon*, ed. RM Canup, K Righter, p. 413. Tucson: Univ. Ariz. Press
- Afonso C, Albert JN, Alard C, Andersen J, Ansari R, et al. 2003. *Astron. Astrophys.* 404:145
- Albrow M, Beaulieu JP, Birch P, Caldwell JAR, Kane S, et al. 1998. *Ap. J.* 509:687
- Alcock C, Akerlof CW, Allsman RA, Axelrod TS, Bennett DP, et al. 1993. *Nature* 365:621
- Alcock C, Allsman RA, Alves D, Axelrod TS, Becker AC, et al. 1996. *Ap. J. Lett.* 463:L67
- Alibert Y, Mordasini C, Benz W. 2011. *Astron. Astrophys.* 526:A63
- Aubourg E, Bareyre P, Bréhin S, Gros M, Lachize-Rey M, et al. 1993. *Nature* 365:623
- Batista V, Gould A, Dieters S, Dong S, Bond I, et al. 2011. *Astron. Astrophys.* 529:A102
- Beaulieu JP, Bennett DP, Batista V, Cassan A, Kubas D, et al. 2010. In *Pathways Towards Habitable Planets*, ed. VC du Foresto, DM Gelino, I Ribas, 430:266. San Francisco: ASP
- Beaulieu JP, Bennett DP, Fouqué P, Williams A, Dominik M, et al. 2006. *Nature* 439:437
- Bennett DP. 2004. In *Extrasolar Planets: Today and Tomorrow*, ed. J-P Beaulieu, A Lecavelier des Etangs, C Terquem. *ASP Conf. Ser.* 321:5. San Francisco: ASP

- Bennett DP. 2008. In *Exoplanets: Detection, Formation, Properties, Habitability*, ed. J. Mason, pp. 47–88. Berlin: Springer
- Bennett DP, Anderson J, Gaudi BS. 2007. *Ap. J.* 660:781
- Bennett DP, Bond IA, Udalski A, Sumi T, Abe F, et al. 2008. *Ap. J.* 684:663
- Bennett DP, Rhie SH. 1996. *Ap. J.* 472:660
- Bennett DP, Rhie SH. 2002. *Ap. J.* 574:985
- Bennett DP, Rhie SH, Nikolaev S, Gaudi BS, Udalski A, et al. 2010. *Ap. J.* 713:837
- Bond IA, Udalski A, Jaroszyński M, Rattenbury NJ, Paczyński B, et al. 2004. *Ap. J. Lett.* 606:L155
- Bonfils X, Delfosse X, Udry S, Forveille T, Mayor M, et al. 2012. *Astron. Astrophys.* In press (arXiv:1111.5019)
- Borucki WJ, Koch D, Basri G, Batalha N, Brown T, et al. 2010. *Science* 327:977
- Boutreux T, Gould A. 1996. *Ap. J.* 462:705
- Cassan A, Kubas D, Beaulieu JP, Dominik M, Horne K, et al. 2012. *Nature* 481:167–69
- Chwolson O. 1924. *Astron. Nachr.* 221:329
- Cumming A, Butler RP, Marcy GW, Vogt SS, Wright JT, Fischer DA. 2008. *Publ. Astron. Soc. Jpn.* 120:531
- Di Stefano R. 1999. *Ap. J.* 512:558
- Di Stefano R. 2008. *Ap. J.* 684:59
- Di Stefano R, Scalzo RA. 1999a. *Ap. J.* 512:564
- Di Stefano R, Scalzo RA. 1999b. *Ap. J.* 512:579
- Dominik M. 1998. *Astron. Astrophys.* 329:361
- Dominik M. 1999. *Astron. Astrophys.* 349:108
- Dominik M. 2006. *MNRAS* 367:669
- Dominik M, Jørgensen UG, Rattenbury NJ, Mathiasen M, Hinse TC, et al. 2010. *Astron. Nachr.* 331:671
- Dong S, Bond IA, Gould A, Kozłowski S, Miyake N, et al. 2009a. *Ap. J.* 698:1826
- Dong S, DePoy DL, Gaudi BS, Gould A, Han C, et al. 2006. *Ap. J.* 642:842
- Dong S, Gould A, Udalski A, Anderson J, Christie GW, et al. 2009b. *Ap. J.* 695:970
- Dong S, Udalski A, Gould A, Reach WT, Christie GW, et al. 2007. *Ap. J.* 664:862
- Eddington AS. 1920. *Space, Time and Gravitation. An Outline of the General Relativity Theory*. Cambridge, UK: Cambridge Univ. Press
- Einstein A. 1936. *Science* 84:506
- Erdl H, Schneider P. 1993. *Astron. Astrophys.* 268:453
- Forveille T, Bonfils X, Lo Curto G, Delfosse X, Udry S, et al. 2011. *Astron. Astrophys.* 526:A141
- Gaudi BS. 1998. *Ap. J.* 506:533
- Gaudi BS. 2010. In *Exoplanets*, ed. S. Seager, p. 79. Tucson: Univ. Ariz. Press
- Gaudi BS, Albrow MD, An J, Beaulieu J-P, Caldwell JAR, et al. 2002. *Ap. J.* 566:463
- Gaudi BS, Bennett DP, Udalski A, Gould A, Christie GW, et al. 2008. *Science* 319:927
- Gaudi BS, Gould A. 1997a. *Ap. J.* 477:52
- Gaudi BS, Gould A. 1997b. *Ap. J.* 486:85
- Gaudi BS, Naber RM, Sackett PD. 1998. *Ap. J. Lett.* 502:L33
- Gorbikov E, Brosch N, Afonso C. 2010. *Astron. Space Sci.* 326:203
- Gould A. 1992. *Ap. J.* 392:442
- Gould A. 1994a. *Ap. J. Lett.* 421:L71
- Gould A. 1994b. *Ap. J. Lett.* 421:L75
- Gould A. 1995. *Ap. J. Lett.* 441:L21
- Gould A. 1996. *Publ. Astron. Soc. Pac.* 108:465
- Gould A. 1999. *Ap. J.* 514:869
- Gould A. 2000a. *Ap. J.* 535:928
- Gould A. 2000b. *Ap. J.* 542:785
- Gould A. 2009. *Astro2010: The Astronomy and Astrophysics Decadal Survey, Science White Papers No. 100*
- Gould A, Dong S, Gaudi BS, Udalski A, Bond IA, et al. 2010. *Ap. J.* 720:1073
- Gould A, Gaucherel C. 1997. *Ap. J.* 477:580
- Gould A, Loeb A. 1992. *Ap. J.* 396:104
- Gould A, Udalski A, An D, Bennett DP, Zhou A-Y, et al. 2006. *Ap. J. Lett.* 644:L37

- Green J, Schechter P, Baltay C, Bean R, Bennett D, et al. 2011. Wide-Field InfraRed Survey Telescope (WFIRST) interim report. *Des. Ref. Mission Interim Rep.*, Sci. Def. Team (arXiv:1108.1374)
- Griest K. 1991. *Ap. J.* 366:412
- Griest K, Safizadeh N. 1998. *Ap. J.* 500:37
- Han C. 2005. *Ap. J.* 629:1102
- Han C. 2006. *Ap. J.* 638:1080
- Han C, Gaudi BS, An JH, Gould A. 2005. *Ap. J.* 618:962
- Han C, Gould A. 1995. *Ap. J.* 447:53
- Han C, Park MG. 2002. *J. Korean Astron. Soc.* 35:35
- Hearnshaw JB, Abe F, Bond IA, Gilmore AC, Itow Y, et al. 2006. *The 9th Asian-Pac. Reg. IAU Meet., Nusa Dua, Bali, Indonesia, 26–29 July 2005*, p. 272. Jawa Barat, Indonesia: Inst. Teknol. Bdg.
- Holz DE, Wald RM. 1996. *Ap. J.* 471:64
- Howard AW, Marcy GW, Johnson JA, Fischer DA, Wright JT, et al. 2010. *Science* 330:653
- Howard CD, Rich RM, Reitzel DB, Koch A, De Proprietary R, et al. 2008. *Ap. J.* 688:1060
- Ida S, Lin DNC. 2004. *Ap. J.* 604:388
- Janczak J, Fukui A, Dong S, Monard LAG, Kozłowski S, et al. 2010. *Ap. J.* 711:731
- Johnson JA, Howard AW, Marcy GW, Bowler BP, Henry GW, et al. 2010. *Publ. Astron. Soc. Pac.* 122:149
- Kennedy GM, Kenyon SJ. 2008. *Ap. J.* 673:502
- Kennedy GM, Kenyon SJ, Bromley BC. 2007. *Astron. Space Sci.* 311:9
- Kervella P, Thévenin F, Di Folco E, Ségransan D. 2004. *Astron. Astrophys.* 426:297
- Khavinson D, Neumann G. 2006. *Proc. Am. Math. Soc.* 134:1077
- Kiraga M, Paczyński B. 1994. *Ap. J.* 430:L101
- Kornet K, Wolf S, Różyńska M. 2006. *Astron. Astrophys.* 458:661
- Kubas D, Beaulieu JP, Bennett DP, Cassan A, Cole A, et al. 2012. *Astron. Astrophys.* 540:78
- Laughlin G, Bodenheimer P, Adams FC. 2004. *Ap. J. Lett.* 612:L73
- Lecar M, Podolak M, Sasselov D, Chiang E. 2006. *Ap. J.* 640:115
- Liebes S. 1964. *Phys. Rev.* 133:835
- Lissauer JJ. 1987. *Icarus* 69:249
- Lodge OJ. 1919. *Nature* 104:354
- Mao S. 2008. *Manch. Microlensing Conf.: The 12th Int. Conf. ANGLES Microlensing Workshop, Manchester, United Kingdom, Jan. 21–25, 2008*. Trieste, Italy: SISSA Proc. Sci. (arXiv:0811.0441)
- Mao S, Paczyński B. 1991. *Ap. J. Lett.* 374:L37
- Mao S, Paczyński B. 1996. *Ap. J.* 473:57
- Mayor M, Marmier M, Lovis C, Udry S, Ségransan D, et al. 2012. *Astron. Astrophys.* Submitted (arXiv:1109.2497)
- Miyake N, Sumi T, Dong S, Street R, Mancini L, et al. 2011. *Ap. J.* 728:120
- Muraki Y, Han C, Bennett DP, Suzuki D, Monard LAG, et al. 2011. *Ap. J.* 741:22
- Paczynski B. 1986. *Ap. J.* 304:1
- Paczynski B. 1996. *Annu. Rev. Astron. Astrophys.* 34:419
- Paczynski B, Stanek KZ. 1998. *Ap. J. Lett.* 494:L219
- Petters AO, Levine H, Wambsganss J. 2001. *Singularity Theory and Gravitational Lensing*. Boston: Birkhäuser
- Pollack JB, Hubickyj O, Bodenheimer P, Lissauer JJ, Podolak M. 1996. *Icarus* 124:62
- Popowski P, Griest K, Thomas CL, Cook KH, Bennett DP, et al. 2005. *Ap. J.* 631:879
- Press WH, Teukolsky SA, Vetterling WT, Flannery BP. 1992. *Numerical Recipes in FORTRAN. The Art of Scientific Computing*. New York: Cambridge Univ. Press
- Refsdal S. 1964. *MNRAS* 128:295
- Refsdal S. 1966. *MNRAS* 134:315
- Renn J, Sauer T, Stachel J. 1997. *Science* 275:184
- Rhie SH, Bennett DP, Becker AC, Peterson BA, Fragile PC, et al. 2000. *Ap. J.* 533:378
- Rivkin AS, Howell ES, Vilas F, Lebofsky LA. 2002. In *Asteroids III*, ed. WF Bottke, A Cellino, P Paolicchi, RP Binzel, p. 235. Tucson: Univ. Ariz. Press
- Sackett PD. 1999. *Planets Outside the Solar System: Theory and Observations*, ed. J-M Mariotti, D Alloin, pp. 189–228. Boston: Kluwer



- Sako T, Sekiguchi T, Sasaki M, Okajima K, Abe F, et al. 2008. *Exp. Astron.* 22:51
- Sauer T. 2008. *Arch. Hist. Exact Sci.* 62:1
- Schneider P, Ehlers J, Falco EE. 1992. *Gravitational Lenses*. Berlin: Springer-Verlag
- Shvartzvald Y, Maoz D. 2011. *MNRAS* 419:3631
- Skowron J, Udalski A, Gould A, Dong S, Monard LAG, et al. 2011. *Ap. J.* 738:87
- Snodgrass C, Horne K, Tsapras Y. 2004. *MNRAS* 351:967
- Sumi T, Bennett DP, Bond IA, Udalski A, Batista V, et al. 2010. *Ap. J.* 710:1641
- Sumi T, Kamiya K, Bennett DP, Bond IA, Abe F, et al. 2011. *Nature* 473:349
- Sumi T, Woźniak PR, Udalski A, Szymanski M, Kubiak M, et al. 2006. *Ap. J.* 636:240
- Tsapras Y, Street R, Horne K, Snodgrass C, Dominik M, et al. 2009. *Astron. Nachr.* 330:4
- Udalski A. 2003. *Acta Astron.* 53:291
- Udalski A. 2009. In *The Variable Universe: A Celebration of Bohdan Paczyński*, *ASP Conf. Ser.* 403:110. San Francisco: ASP
- Udalski A, Jaroszyński M, Paczyński B, Kubiak M, Szymański MK, et al. 2005. *Ap. J. Lett.* 628:L109
- Udalski A, Szymanski M, Kaluzny J, Kubiak M, Krzeminski W, et al. 1993. *Acta Astron.* 43:289
- Udalski A, Szymanski M, Kaluzny J, Kubiak M, Mateo M, et al. 1994. *Acta Astron.* 44:227
- Wambsganss J. 1997. *MNRAS* 284:172
- Witt HJ. 1990. *Astron. Astrophys.* 236:311
- Witt HJ, Mao S. 1995. *Ap. J.* 447:L105
- Yee JC, Shvartzvald Y, Gal-Yam A, Bond IA, Udalski A, et al. 2012. *Ap. J.* In press (arXiv:1201.1002)
- Yoo J, DePoy DL, Gal-Yam A, Gaudi BS, Gould A, et al. 2004. *Ap. J.* 603:139



# Contents

Seeing Cosmology Grow <i>P. J. E. Peebles</i> .....	1
Magnetic Fields in Molecular Clouds <i>Richard M. Crutcher</i> .....	29
The Formation and Early Evolution of Low-Mass Stars and Brown Dwarfs <i>Kevin L. Luhman</i> .....	65
Presupernova Evolution of Massive Single and Binary Stars <i>N. Langer</i> .....	107
Critical Reactions in Contemporary Nuclear Astrophysics <i>M. Wiescher, F. Käppeler, and K. Langanke</i> .....	165
Planet-Disk Interaction and Orbital Evolution <i>W. Kley and R. P. Nelson</i> .....	211
Galactic Stellar Populations in the Era of the Sloan Digital Sky Survey and Other Large Surveys <i>Željko Ivezić, Timothy C. Beers, and Mario Jurić</i> .....	251
Adaptive Optics for Astronomy <i>R. Davies and M. Kasper</i> .....	305
Formation of Galaxy Clusters <i>Andrey V. Kravtsov and Stefano Borgani</i> .....	353
Microlensing Surveys for Exoplanets <i>B. Scott Gaudi</i> .....	411
Observational Evidence of Active Galactic Nuclei Feedback <i>A. C. Fabian</i> .....	455
Gaseous Galaxy Halos <i>M. E. Putman, J. E. G. Peek, and M. R. Young</i> .....	491

Star Formation in the Milky Way and Nearby Galaxies <i>Robert C. Kennicutt Jr. and Neal J. Evans II</i> .....	531
Thermonuclear Burst Oscillations <i>Anna L. Watts</i> .....	609

## Indexes

Cumulative Index of Contributing Authors, Volumes 39–50 .....	641
Cumulative Index of Chapter Titles, Volumes 39–50 .....	644

## Errata

An online log of corrections to *Annual Review of Astronomy and Astrophysics* articles may be found at <http://astro.annualreviews.org/errata.shtml>